K-matrix formulation of two-particle scattering in a waveguide in the presence of one-dimensional spin-orbit coupling

Su-Ju Wang, Q. Guan, and D. Blume

Phys. Rev. A **98**, 022708 — Published 31 August 2018

DOI: 10.1103/PhysRevA.98.022708

K-matrix formulation of two-particle scattering in a wave guide in the presence of one-dimensional spin-orbit coupling

Su-Ju Wang,* Q. Guan,† and D. Blume‡
Homer L. Dodge Department of Physics and Astronomy, The University of Oklahoma, 440 West Brooks Street, Norman, Oklahoma 73019, USA
(Dated: August 6, 2018)

The creation of artificial gauge fields in neutral ultracold atom systems has opened the possibility to study the effects of spin-orbit coupling terms in clean environments. This work considers the multi-channel scattering properties of two atoms confined by a wave guide in the presence of spin-orbit coupling terms within a K-matrix scattering framework. The tunability of resonances, induced by the interplay of the external wave guide geometry, the interactions, and the spin-orbit coupling terms, is demonstrated. Our results for the K-matrix elements as well as partial and total reflection coefficients for two identical fermions interacting through a finite-range interaction potential in the singlet channel only are compared with those obtained for a strictly one-dimensional effective low-energy Hamiltonian, which uses the effective coupling constant derived in Zhang *et al.* [Scientific Reports **4**, 1 (2014)] and Zhang *et al.* [Phys. Rev. A **88**, 053605 (2013)] as input. In the regime where the effective Hamiltonian is applicable, good agreement is obtained, provided the energy-dependence of the coupling constant is accounted for. Our approach naturally describes the energy regime in which the bands associated with excited transverse modes lie below a subset of the bands associated with the lowest transverse modes. The threshold behavior is discussed and scattering observables are linked to bound state properties.

PACS numbers:

I. INTRODUCTION

Confinement-induced two-atom resonances occur when the length scale that characterizes the outcome of the low energy collision between two atoms in free space is comparable to the size of the tight confinement length [1–3]. For a wave guide geometry with harmonic confinement in the x- and y-directions, the asymptotic even- or odd-z solutions along the wave guide direction (z-direction) are the result of a multi-channel scattering calculation. Since the energetically closed channels are accessible during the collision process, the effective one-dimensional even- and odd-z coupling constants can be understood as being renormalized by the energetically closed channels [1, 4, 5]. The K-matrix formalism ($\underline{K}$ is the reaction matrix) has been shown to provide a transparent description of such multi-channel problems [5–7].

The present paper addresses what happens when the colliding atoms are additionally feeling one-dimensional spin-orbit coupling terms (equal mixture of Rashba and Dresselhaus spin-orbit coupling) [8–11]. Among the various spin-orbit coupling schemes that have been realized experimentally by now [12–18], the one-dimensional spin-orbit coupling considered in this work is the most common. Our work revisits the case where the spin-orbit coupling direction is oriented along the wave guide axis [19, 20]. A multi-channel K-matrix scattering theory that accounts for the modification of the asymptotic solution due to the spin-orbit coupling is developed. Our theoretical framework is applied to two identical fermions with finite-range interaction in the singlet channel. The theory is also applicable to two identical bosons, and to distinguishable particles with spin-dependent interactions. It is found that even a relatively weak spin-orbit coupling strength can lead to significant modifications of the resonance structure that one would obtain in the absence of spin-orbit coupling, thus providing an alternative route for controlling two-body resonances in a wave guide geometry.

The interplay between the external confinement and the spin-orbit coupling terms has already been explored in two previous publications [19, 20] for two identical fermions interacting via zero-range interactions in the singlet channel and vanishing interactions in the triplet channels. Where comparisons can be made, our results are in agreement with these earlier results. The framework developed here is, however, more general in that it is applicable to any type of interaction and any number of open channels. The accomplishments of our work are:

- A general scattering framework applicable to two-particle scattering in the presence of an external two-dimensional harmonic trap and one-dimensional spin-orbit coupling terms is developed.
- The "rotation approach", introduced in Refs. [21, 22], is generalized to the wave guide problem and used to interpret a subset of the results.
- The effective one-dimensional coupling constant, derived in Ref. [19] in terms of a two-dimensional integral (see also Ref. [20]), is found to be well approximated by the Hurwitz-Zeta function in cer-

*Electronic address: sjwang@ou.edu
†Electronic address: gqz0001@gmail.com
‡Electronic address: doerte.blume-1@ou.edu

tain parameter regimes. A physical picture of the energy-dependence of the Hurwitz-Zeta function is provided.

- The effective low-energy Hamiltonian is validated and K-matrix results are also presented in the energy regime, in which the effective low-energy Hamiltonian from the literature [19, 20] is invalid.

- The threshold laws in the vicinity of various scattering thresholds are derived and interpreted.

- The tunability of the scattering resonances is demonstrated and interpreted for two identical fermions.

The remainder of this paper is structured as follows. Section II introduces the system Hamiltonian and recasts, taking advantage of the symmetries of the system, the associated Schrödinger equation in matrix form. The scattering solutions of the matrix equation in the inner region are obtained using the generalized log-derivative algorithm [23, 24], which works when the usual second derivative operators are complemented by first derivative operators; in our case, these arise from the spin-orbit coupling terms. A discussion of the generalized log-derivative algorithm is relegated to Appendix A. Section III discusses the asymptotic solution that the inner solution is being matched to as well as the extraction of the physical K-matrix via channel elimination. Taking a step back, Sec. IV introduces an alternative approximate "rotation approach" that recasts the coupled-channel problem in such a way that the first derivative operators are rotated away. This facilitates the use of standard algorithms such as the Johnson algorithm [25], thus vastly simplifying the numerics, and provides a theoretical framework within which to interpret the scattering results, at least in some parameter regimes. The effective one-dimensional coupling constant [19, 20], which enters into the effective 4×4 low-energy Hamiltonian, is introduced in Sec. V and the associated threshold laws are analyzed. Section VI applies the developed theory to two identical fermions. Scattering quantities such as the partial and total reflection coefficients are analyzed as a function of the scattering energy. To aid with the interpretation of the scattering observables, we also calculate the corresponding two-fermion bound states. Last, Sec. VII provides a summary and an outlook.

II. SET-UP OF THE PROBLEM

We consider two identical point particles with mass m that feel the single-particle Rashba-Dresselhaus spin-orbit coupling $\hat{V}_{\mathrm{so},j}$ ($j = 1$ and 2) [10, 11],

$$\hat{V}_{\mathrm{so},j} = \frac{\hbar k_{\mathrm{so}} \hat{p}_{j,z}}{m} \hat{\sigma}_{j,z} + \frac{\hbar\Omega}{2} \hat{\sigma}_{j,x} + \frac{\hbar\delta}{2} \hat{\sigma}_{j,z}, \tag{1}$$

as well as the single-particle harmonic potential $\hat{V}_{\mathrm{trap},j}$ in the transverse directions,

$$\hat{V}_{\mathrm{trap},j} = \frac{1}{2} m\omega^2 \rho_j^2. \tag{2}$$

Here, k_{so} is the strength of the spin-orbit coupling, Ω the Raman coupling strength, δ the detuning, and ω the angular trapping frequency. The position vectors of the particles are denoted by $\vec{r}_j$ (with components x_j, y_j, and z_j) and the single-particle momentum operators by $\hat{\vec{p}}_j$ (with components $\hat{p}_{j,x}$, $\hat{p}_{j,y}$, and $\hat{p}_{j,z}$). The quantity ρ_j is defined through $\rho_j^2 = x_j^2 + y_j^2$. The spin-orbit coupling assumes that each atom can be considered as containing two energy levels that form an effective spin-1/2 system, described by the three Pauli matrices $\hat{\sigma}_{j,x}$, $\hat{\sigma}_{j,y}$, and $\hat{\sigma}_{j,z}$. This type of spin-orbit coupling is nowadays being realized routinely in cold atom systems [13, 26–31]. In addition to the single-particle potentials, the particles feel a spin-dependent two-body interaction potential $\hat{V}_{\mathrm{int}}$,

$$\begin{aligned} \hat{V}_{\mathrm{int}} = \quad & V_{S_0}(\vec{r})|S_0\rangle\langle S_0| + V_{T_{+1}}(\vec{r})|T_{+1}\rangle\langle T_{+1}| + \\ & V_{T_{-1}}(\vec{r})|T_{-1}\rangle\langle T_{-1}| + V_{T_0}(\vec{r})|T_0\rangle\langle T_0|. \end{aligned} \tag{3}$$

For identical particles, the interaction between the spin-up state of the first atom and the spin-down state of the second atom is equal to the interaction between the spin-down state of the first atom and the spin-up state of the second atom. This implies: $V_{S_0}(\vec{r}) = V_{T_0}(\vec{r}) = V_0(\vec{r})$. The interaction potential is written using the singlet-triplet basis states

$$|S_0\rangle = \frac{1}{\sqrt{2}} \left(|\uparrow\downarrow\rangle - |\downarrow\uparrow\rangle \right), \tag{4}$$

$$|T_{+1}\rangle = |\uparrow\uparrow\rangle, \tag{5}$$

$$|T_{-1}\rangle = |\downarrow\downarrow\rangle, \tag{6}$$

and

$$|T_0\rangle = \frac{1}{\sqrt{2}} \left(|\uparrow\downarrow\rangle + |\downarrow\uparrow\rangle \right), \tag{7}$$

where "$|\uparrow\rangle$" and "$|\downarrow\rangle$" denote the two internal states of the atoms. Throughout this article, the potentials $V_{S_0}(\vec{r})$, $V_{T_{+1}}(\vec{r})$, $V_{T_{-1}}(\vec{r})$, and $V_{T_0}(\vec{r})$ ($\vec{r}$ denotes the distance vector, $\vec{r} = \vec{r}_1 - \vec{r}_2$) are parametrized by spherically-symmetric short-range potentials with range r_0. The use of model interactions like the Gaussian potential is justified if r_0 is notably smaller than the other length scales such as the transverse confinement length of the Hamiltonian. Unless stated otherwise, the ordering of the spin states given in Eqs. (4)-(7) is used in the remainder of this article.

Denoting the kinetic energy $\hat{\vec{p}}_j^2/(2m)$ of the j-th particle by $\hat{T}_j$, the system Hamiltonian $\hat{H}$ reads

$$\begin{aligned} \hat{H} = & \left(\hat{T}_1 + \hat{T}_2 + \hat{V}_{\mathrm{trap},1} + \hat{V}_{\mathrm{trap},2} \right) \hat{I}_1 \otimes \hat{I}_2 + \\ & \hat{V}_{\mathrm{so},1} \otimes \hat{I}_2 + \hat{I}_1 \otimes \hat{V}_{\mathrm{so},2} + \hat{V}_{\mathrm{int}}, \end{aligned} \tag{8}$$

where $\hat{I}_j$ is the identity matrix of the spin Hilbert space of the j-th particle. It can be readily checked that the z-component $\hat{P}_z$ of the total momentum operator $\hat{\vec{P}}$,

$$\hat{\vec{P}} = \hat{\vec{p}}_1 + \hat{\vec{p}}_2, \tag{9}$$

commutes with the total Hamiltonian $\hat{H}$ [32]. This implies that the expectation value P_z of the operator $\hat{P}_z$ is a good quantum number and that the Schrödinger equation for the Hamiltonian $\hat{H}$ can be solved separately for each P_z [19, 20]. Using this, we separate $\hat{H}$ into the center-of-mass Hamiltonian $\hat{H}_{\rm cm}$ and the relative Hamiltonian $\hat{H}_{\rm rel}$ [19, 20],

$$\hat{H} = \hat{H}_{\rm cm} + \hat{H}_{\rm rel}. \tag{10}$$

We have

$$\hat{H}_{\rm cm} = \frac{P_z^2}{2M}\hat{I}_1 \otimes \hat{I}_2 + \left(\frac{\hat{P}_x^2 + \hat{P}_y^2}{2M} + \frac{1}{2}M\omega^2(X^2+Y^2)\right)\hat{I}_1 \otimes \hat{I}_2 \tag{11}$$

and

$$\hat{H}_{\rm rel} = \hat{H}_{\rm ho} + \hat{T}_{{\rm rel},z} + \hat{V}_{\rm int} + \hat{V}_{\rm so}, \tag{12}$$

where

$$\hat{H}_{\rm ho} = \left(\frac{\hat{p}_x^2 + \hat{p}_y^2}{2\mu} + \frac{1}{2}\mu\omega_\perp^2\rho^2\right)\hat{I}_1 \otimes \hat{I}_2, \tag{13}$$

$$\hat{T}_{{\rm rel},z} = \frac{\hat{p}_z^2}{2\mu}\hat{I}_1 \otimes \hat{I}_2, \tag{14}$$

and

$$\hat{V}_{\rm so} = \frac{\hbar k_{\rm so}}{\mu}\hat{p}_z\hat{\Sigma}_z + \frac{\hbar\Omega}{2}(\hat{\sigma}_{1,x}\otimes\hat{I}_2 + \hat{I}_1\otimes\hat{\sigma}_{2,x}) + \frac{\hbar\tilde{\delta}}{2}(\hat{\sigma}_{1,z}\otimes\hat{I}_2 + \hat{I}_1\otimes\hat{\sigma}_{2,z}) \tag{15}$$

with

$$\hat{\Sigma}_z = \frac{1}{2}\left(\hat{\sigma}_{1,z}\otimes\hat{I}_2 - \hat{I}_1\otimes\hat{\sigma}_{2,z}\right) \tag{16}$$

and

$$\frac{\hbar\tilde{\delta}}{2} = \frac{\hbar\delta}{2} + \frac{\hbar k_{\rm so}P_z}{M}. \tag{17}$$

Here, M and μ denote the total mass and reduced mass, respectively, and the center-of-mass vector $\vec{R}$ has the components X, Y, and Z. The relative momentum operator is denoted by $\hat{\vec{p}}$ and ρ^2 is defined through x^2+y^2. Note that $\hat{V}_{\rm so}$ depends on the operator $\hat{p}_z$ but not on the operator $\hat{P}_z$ ($\hat{P}_z$ is replaced by P_z). Since the center-of-mass momentum P_z can, according to Eq. (17), be interpreted as "changing" the physical detuning δ, we refer to $\tilde{\delta}$ as an effective or generalized detuning [33]. The center-of-mass Hamiltonian $\hat{H}_{\rm cm}$ is identical to the two-dimensional harmonic oscillator Hamiltonian for a particle of mass M, with the motion in the third dimension being governed by the free-particle Hamiltonian. The eigen states and eigen energies of the corresponding Schrödinger equation can be written down readily. In what follows, we focus on the solutions to the Schrödinger equation for the relative Hamiltonian $\hat{H}_{\rm rel}$.

To solve the relative Schrödinger equation, we use that the z-component $\hat{l}_z$ of the orbital angular momentum operator $\vec{l}$ associated with the relative distance vector $\vec{r}$ commutes with $\hat{H}_{\rm rel}$, i.e., $[\hat{l}_z, \hat{H}_{\rm rel}] = 0$. This implies that we can determine the eigen states of $\hat{H}_{\rm rel}$ separately for each m_l, where m_l is the quantum number associated with $\hat{l}_z$; m_l takes the values $0, \pm 1, \cdots$. We expand the eigen states $\Psi^{(m_l)}$ of $\hat{H}_{\rm rel}$ for fixed m_l as follows:

$$\Psi^{(m_l)} = \sum_{n_\rho,\chi}\phi^{(m_l)}_{n_\rho,\chi}(z)\Phi^{(m_l)}_{n_\rho}(\rho)|\chi\rangle, \tag{18}$$

where the channel functions $\Phi^{(m_l)}_{n_\rho}(\rho)|\chi\rangle$ are eigen states of $\hat{H}_{\rm ho}$ with eigen energies ϵ_{n_ρ,m_l},

$$\epsilon_{n_\rho,m_l} = (2n_\rho + |m_l| + 1)\hbar\omega. \tag{19}$$

The radial quantum number n_ρ takes the values $n_\rho = 0, 1, \cdots, n_{\rm max}-1$, where $n_{\rm max}$ is the number of $\Phi^{(m_l)}_{n_\rho}$ included in the expansion. The $\Phi^{(m_l)}_{n_\rho}(\rho)$ are, of course, just the two-dimensional harmonic oscillator functions. The index χ in Eq. (18) runs over the spin functions: $|\chi\rangle = |S_0\rangle$, $|T_{\pm1}\rangle$, and $|T_0\rangle$. The "weight functions" $\phi^{(m_l)}_{n_\rho,\chi}(z)$ are determined by plugging Eq. (18) into the relative Schrödinger equation $\hat{H}_{\rm rel}\Psi^{(m_l)} = E\Psi^{(m_l)}$, where E denotes the relative scattering energy, and solving the resulting set of coupled differential equations,

$$\left(\epsilon_{n_\rho,m_l} + \hat{T}_{{\rm rel},z} - E\right)\phi^{(m_l)}_{n_\rho,\chi}(z) = -\sum_{n'_\rho}\mathcal{V}^{n_\rho,n'_\rho,\chi}_{\rm int}(z)\phi^{(m_l)}_{n'_\rho,\chi}(z) - \sum_{\chi'}\mathcal{V}^{\chi,\chi'}_{\rm so}(\hat{p}_z)\phi^{(m_l)}_{n_\rho,\chi'}(z). \tag{20}$$

The matrix elements $\mathcal{V}^{n'_\rho,n_\rho,\chi}_{\rm int}(z)$ are given by

$$\mathcal{V}^{n'_\rho,n_\rho,\chi}_{\rm int}(z) = \langle\Phi^{(m_l)}_{n'_\rho,\chi}|V_\chi|\Phi^{(m_l)}_{n_\rho,\chi}\rangle, \tag{21}$$

where V_χ is equal to V_{S_0}, $V_{T_{\pm1}}$, and V_{T_0} for $|\chi\rangle = |S_0\rangle$ $|T_{\pm1}\rangle$, and $|T_0\rangle$, respectively. The matrix elements $\mathcal{V}^{\chi',\chi}_{\rm so}(\hat{p}_z)$ are given by

$$\mathcal{V}^{\chi',\chi}_{\rm so}(\hat{p}_z) = \langle\chi'|\hat{V}_{\rm so}|\chi\rangle. \tag{22}$$

In deriving the coupled equations given in Eq. (20), we used that the interaction potential $\hat{V}_{\rm int}$ is diagonal in the singlet-triplet basis (it couples different n_ρ) and that the

spin-orbit coupling term $\hat{V}_{\rm so}$ is diagonal in the harmonic oscillator basis states (it couples different χ).

In practice, we solve the coupled equations by rewriting Eq. (20) as a matrix of dimension $(4n_{\rm max})\times(4n_{\rm max})$ (we denote the matrix by $\underline{H}_{\rm rel}$) acting on the vector

$$\vec{\phi}^{(m_l)} = (\phi_{0,S_0}^{(m_l)}(z), \phi_{0,T_{+1}}^{(m_l)}(z), \cdots, \phi_{n_{\rm max}-1,T_0}^{(m_l)}(z))^T. \quad (23)$$

Since the resulting equation $\underline{H}_{\rm rel}\vec{\phi}^{(m_l)} = E\vec{\phi}^{(m_l)}$ has $4n_{\rm max}$ linearly independent solutions, we construct the matrix $\underline{\phi}^{(m_l)}$, which contains the j-th eigen vector $\vec{\phi}^{(m_l)}$ in the j-th column, and solve the resulting matrix equation

$$\underline{H}_{\rm rel}\underline{\phi}^{(m_l)} = E\underline{\phi}^{(m_l)} \quad (24)$$

numerically for relative energies E equal to or greater than the energy $E_{\rm th}$ of the scattering threshold [see Eq. (42) for an actual expression for $E_{\rm th}$]. The details for enforcing the small-$|z|$ boundary condition and the algorithm for determining the logarithmic derivative matrix $\underline{\mathcal{Y}}(z)$,

$$\underline{\mathcal{Y}}(z) = \frac{d\underline{\phi}^{(m_l)}}{dz}\left(\underline{\phi}^{(m_l)}\right)^{-1}, \quad (25)$$

are discussed in Appendix A.

Our goal in this work is to determine the scattering solutions of the relative Hamiltonian $\hat{H}_{\rm rel}$ and to extract scattering observables from it. To this end, the numerically obtained logarithmic derivative matrix $\underline{\mathcal{Y}}(z)$ needs to be matched to the corresponding asymptotic large-$|z|$ solution, i.e., to the solution obtained for $\hat{V}_{\rm int} = 0$. Once the matching is done, the energetically closed channels need to be eliminated. The next section details these steps.

III. SCATTERING FRAMEWORK

A. Asymptotic solution

The goal of this subsection is to determine the asymptotic large-$|z|$ solutions, which are obtained by setting $\hat{V}_{\rm int}$ to zero. It follows from the discussion in Sec. II that different n_ρ channels are decoupled in the absence of interactions. This implies that the Hamiltonian matrix $\underline{H}_{\rm rel,ni}$, which is identical to $\underline{H}_{\rm rel}$ except that the matrix elements $\mathcal{V}_{\rm int}^{n'_\rho,n_\rho,\chi}(z)$ are zero, is block diagonal, with each fixed n_ρ-block having dimension 4×4. To write down the full solution, we solve one of the 4×4 blocks for fixed scattering energy E and arbitrary n_ρ. In writing down the asymptotic solution, we assume that m_l is even and drop the m_l superscript for notational simplicity. The changes required for odd m_l are indicated in the text.

We denote the regular and irregular solutions of the 4×4 block by $\underline{f}_{n_\rho}$ and $\underline{g}_{n_\rho}$, respectively. The 4×4 matrix $\underline{f}_{n_\rho}$ contains the eigen vector $\vec{f}_{n_\rho}^{(j)}$ in the j-th column (and similarly for the irregular solution). To obtain $\vec{f}_{n_\rho}^{(j)}$ and $\vec{g}_{n_\rho}^{(j)}$, we make the ansatz

$$\vec{f}_{n_\rho}^{(j)} = \begin{pmatrix} a_1^{(j)}(k_{n_\rho}^{(j)})\mathcal{A}(k_{n_\rho}^{(j)}|z|) \\ \imath a_2^{(j)}(k_{n_\rho}^{(j)})\mathcal{B}(k_{n_\rho}^{(j)}|z|) \\ \imath a_3^{(j)}(k_{n_\rho}^{(j)})\mathcal{B}(k_{n_\rho}^{(j)}|z|) \\ \imath a_4^{(j)}(k_{n_\rho}^{(j)})\mathcal{B}(k_{n_\rho}^{(j)}|z|) \end{pmatrix}\Phi_{n_\rho}(\rho) \quad (26)$$

and

$$\vec{g}_{n_\rho}^{(j)} = \begin{pmatrix} a_1^{(j)}(k_{n_\rho}^{(j)})\mathcal{C}(k_{n_\rho}^{(j)}|z|) \\ \imath a_2^{(j)}(k_{n_\rho}^{(j)})\mathcal{D}(k_{n_\rho}^{(j)}|z|) \\ \imath a_3^{(j)}(k_{n_\rho}^{(j)})\mathcal{D}(k_{n_\rho}^{(j)}|z|) \\ \imath a_4^{(j)}(k_{n_\rho}^{(j)})\mathcal{D}(k_{n_\rho}^{(j)}|z|) \end{pmatrix}\Phi_{n_\rho}(\rho), \quad (27)$$

where

$$\mathcal{A}(k_{n_\rho}^{(j)}|z|) = \begin{cases} \cos(k_{n_\rho}^{(j)}|z|) \text{ for FF } (m_l \text{ even}) \\ \text{sign}(z)\sin(k_{n_\rho}^{(j)}|z|) \text{ for BB } (m_l \text{ even}) \end{cases}, \quad (28)$$

$$\mathcal{B}(k_{n_\rho}^{(j)}|z|) = \begin{cases} \text{sign}(z)\sin(k_{n_\rho}^{(j)}|z|) \text{ for FF } (m_l \text{ even}) \\ -\cos(k_{n_\rho}^{(j)}|z|) \text{ for BB } (m_l \text{ even}) \end{cases}, \quad (29)$$

$$\mathcal{C}(k_{n_\rho}^{(j)}|z|) = \begin{cases} \sin(k_{n_\rho}^{(j)}|z|) \text{ for FF } (m_l \text{ even}) \\ -\text{sign}(z)\cos(k_{n_\rho}^{(j)}|z|) \text{ for BB } (m_l \text{ even}) \end{cases}, \quad (30)$$

and

$$\mathcal{D}(k_{n_\rho}^{(j)}|z|) = \begin{cases} -\text{sign}(z)\cos(k_{n_\rho}^{(j)}|z|) \text{ for FF } (m_l \text{ even}) \\ -\sin(k_{n_\rho}^{(j)}|z|) \text{ for BB } (m_l \text{ even}) \end{cases}. \quad (31)$$

In Eqs. (26)-(31), the spatial parts are chosen such that the components of $\vec{f}_{n_\rho}^{(j)}$ and $\vec{g}_{n_\rho}^{(j)}$ have the correct symmetry for two identical fermions (FF) and two identical bosons (BB). Specifically, the spin singlet state is antisymmetric under the exchange of the spins of the first and second particles. Thus, the corresponding spatial part for two identical fermions has to be symmetric under the exchange of the spatial degrees of freedom while that for two identical bosons has to be anti-symmetric. Since m_l is assumed to be even, the functions Φ_{n_ρ} are unchanged when exchanging the spatial coordinates of the particles. This implies that the functions $\mathcal{A}$ and $\mathcal{C}$ have to be even for two identical fermions and odd for two identical bosons. The argument for the spin triplet components follows the same logic.

The $k_{n_\rho}^{(j)}$ are defined in terms of the scattering energy E,

$$E = \epsilon_{n_\rho,m_l} + E_z^{(j)}(\hbar k_{n_\rho}^{(j)}), \quad (32)$$

where the $E_z^{(j)}$ are the four relative free-particle dispersion curves. The dispersion curves are obtained by solving a quartic equation in $E_z^{(j)}$. One finds [34]

$$E_z^{(1/2)}(p_z) = \frac{p_z^2}{m} \pm \sqrt{2a - 2\sqrt{a^2 - \frac{p_z^2}{m} E_{\rm so} E_{\tilde{\delta}}^2}} \quad (33)$$

and

$$E_z^{(3/4)}(p_z) = \frac{p_z^2}{m} \pm \sqrt{2a + 2\sqrt{a^2 - \frac{p_z^2}{m} E_{\rm so} E_{\tilde{\delta}}^2}}, \quad (34)$$

where

$$a = \frac{p_z^2}{m} E_{\rm so} + \frac{1}{4}\left(E_\Omega^2 + E_{\tilde{\delta}}^2\right). \quad (35)$$

Here, we defined

$$E_\Omega = \hbar\Omega, \quad (36)$$

$$E_{\rm so} = \frac{\hbar^2 k_{\rm so}^2}{m}, \quad (37)$$

and

$$E_{\tilde{\delta}} = \hbar\tilde{\delta}. \quad (38)$$

The plus and minus signs in Eq. (33) are for $E_z^{(1)}(p_z)$ and $E_z^{(2)}(p_z)$, respectively. The plus and minus signs in Eq. (34) are for $E_z^{(3)}(p_z)$ and $E_z^{(4)}(p_z)$, respectively. Explicit expressions for the vectors $\vec{a}^{(j)}$ for $\tilde{\delta} = 0$ are reported in Appendix B.

For odd m_l, the asymptotic solutions for two identical fermions given above become the solutions for two identical bosons, and vice versa. For two distinguishable particles, no symmetry constraints exist, implying that the "bosonic" and "fermionic" solutions need to be combined.

Having the regular 4×4 matrix solutions $\underline{f}_{n_\rho}$, we define the matrix $\underline{f}$ through

$$\underline{f} = \begin{pmatrix} \underline{f}_0 & 0 & \cdots & 0 \\ 0 & \underline{f}_1 & & \\ \vdots & & \ddots & \\ 0 & & & \underline{f}_{n_{\rm max}-1} \end{pmatrix}. \quad (39)$$

The matrix $\underline{g}$ is defined analogously. With these definitions, the asymptotic large-$|z|$ solution $\underline{\Psi}_{\rm out}$ reads

$$\underline{\Psi}_{\rm out} = \underline{f} - \underline{g}\underline{K}. \quad (40)$$

The K-matrix is obtained by equating the inner solution $\underline{\Psi}$ and the outer solution $\underline{\Psi}_{\rm out}$ as well as their derivatives with respect to z at $z = z_{\rm max}$, where $z_{\rm max}$ is chosen such that the inner solution $\underline{\Psi}$ has reached its asymptotic behavior, i.e., such that the phase accumulation due to the interaction potential has reached a converged value. In terms of the logarithmic derivative matrix $\underline{\mathcal{Y}}(z)$ at $z_{\rm max}$ [see Eq. (25)], the K-matrix can be written as [21]

$$\underline{K} = \left[\underline{\mathcal{Y}}(z)\underline{g}(z) - \frac{d\underline{g}(z)}{dz}\right]^{-1}\left[\underline{\mathcal{Y}}(z)\underline{f}(z) - \frac{d\underline{f}(z)}{dz}\right]_{z=z_{\rm max}}. \quad (41)$$

Figures 1(a) and 1(b) show the relative dispersion curves $E_z^{(j)}(p_z)$ as a function of the relative wave vector k_z in the z-direction, which is defined as $k_z = p_z/\hbar$, for $\tilde{\delta} = 0$ in the double-minimum regime ($E_\Omega = E_{\rm so}$) and in the single-minimum regime ($E_\Omega = 5E_{\rm so}/2$), respectively. For $\tilde{\delta} = 0$, the transition from the double-minimum to the single-minimum regime occurs at $\hbar\Omega_* = 2E_{\rm so}$. The minimum of the lowest dispersion curve defines the scattering threshold $E_{\rm th}$,

$$E_{\rm th} = \min_{p_z,j}\left(E_z^{(j)}(p_z) + \hbar\omega\right). \quad (42)$$

For $\tilde{\delta} = 0$, one finds

$$E_{\rm th} = \begin{cases} \hbar\omega - E_{\rm so} - \frac{(E_\Omega)^2}{4E_{\rm so}} & \text{for } \Omega < \Omega_* \\ \hbar\omega - E_\Omega & \text{for } \Omega > \Omega_* \end{cases}. \quad (43)$$

Scattering solutions are obtained for energies E equal to or greater than $E_{\rm th}$. Inspection of Eqs. (32)-(35) shows that the $k_{n_\rho}^{(j)}$ can be imaginary (whether or not they are imaginary depends on the values of E, $E_{\rm so}$, E_Ω, $E_{\tilde{\delta}}$, and $\hbar\omega$). If a $k_{n_\rho}^{(j)}$ is imaginary, the solution blows up exponentially at large $|z|$ in the respective channel. Physically, the channel is energetically closed and needs to be eliminated. The next subsection illustrates how the energetically closed channels are eliminated to obtain the physical K-matrix $\underline{K}_{\rm phys}$.

Figure 2 shows the probability P_χ that the state corresponding to the lowest scattering threshold for $\tilde{\delta} = 0$ is in the spin channel $|\chi\rangle$ as a function of $E_\Omega/E_{\rm so}$. As Ω increases from zero to Ω_* [Fig. 2(a)], the spin composition changes quite a bit. For $\Omega > \Omega_*$ [Fig. 2(b)], in contrast, the spin composition of the scattering threshold is constant. For infinitesimally small Ω, the state corresponding to the lowest scattering threshold contains predominantly $|S_0\rangle$ and $|T_0\rangle$ admixtures. The $|S_0\rangle$ contribution decreases to zero as Ω reaches Ω_* and remains zero for $\Omega > \Omega_*$. The spin-composition of the state at the lowest scattering threshold is used in Sec. VI to interpret the scattering observables. The second lowest scattering threshold is two-fold degenerate. Importantly, one of the associated states is a pure $|S_0\rangle$ state for all Ω and the other is a superposition of the $|T_{+1}\rangle$ and $|T_{-1}\rangle$ channels. The fact that one of the two second lowest threshold states corresponds to the $|S_0\rangle$ channel plays an important role in understanding the resonance structure for $\Omega > \Omega_*$.

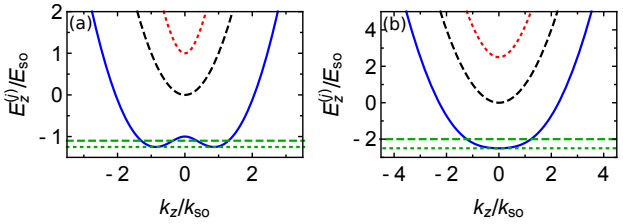

FIG. 1: (color online) Non-interacting relative dispersion curves $E_z^{(j)}$ as a function of k_z/k_{so} for $\tilde{\delta}=0$ and (a) $E_\Omega = E_{so}$ (double-minimum regime) and (b) $E_\Omega = 5E_{so}/2$ (single-minimum regime). The green dotted horizontal lines depict E_{th} [Eq. (43)]. The green dashed horizontal lines depict a scattering energy E for which the number of energetically open channels, assuming $2\hbar\omega$ is larger than the difference between E and E_{th}, is (a) two and (b) one. The discussion of the threshold laws in Sec. V B uses the "Roman labeled" energies E_I, E_{II}, $E_{II'}$, E_{III}, and E_{IV}. The energy E_I is equal to E_{th} for the double-minimum case. The energy E_{II} is equal to E_{th} for the single-minimum case. The energy $E_{II'}$ is given by the local maximum of the blue solid line in the double-minimum regime, $E_{II'} = \hbar\omega - E_\Omega$. The minima of the black dashed and red dotted curves have the energies $E_{III} = \hbar\omega$ and $E_{IV} = \hbar\omega + E_\Omega$, respectively. Assuming $2\hbar\omega$ is larger than $E_{so} + E_\Omega + E_\Omega^2/(4E_{so})$, the number of energetically open channels changes from two to one at $E_{II'}$, from one to three at E_{III}, and from three to four at E_{IV}.

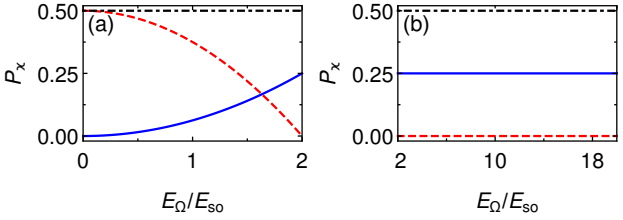

FIG. 2: (color online) Spin composition of the state corresponding to the lowest scattering threshold for $\tilde{\delta}=0$ as a function of E_Ω/E_{so} for (a) $E_\Omega < 2E_{so}$ (double-minimum regime) and (b) $E_\Omega > 2E_{so}$ (single-minimum regime). The probabilities P_χ to be in the $|S_0\rangle$, $|T_0\rangle$, and $|T_{+1}\rangle$ channels are shown by red dashed, black dash-dotted, and blue solid lines, respectively. The probability to be in the $|T_{-1}\rangle$ channel (not shown) is equal to the probability to be in the $|T_{+1}\rangle$ channel.

B. Physical K-matrix

To perform the channel elimination [5–7, 35–38], we partition $\underline{\Psi}_{out}$, $\underline{f}$, $\underline{g}$, and $\underline{K}$ into four blocks: the open-open ("oo"), open-closed ("oc"), closed-open ("co"), and closed-closed ("cc") blocks. To perform this partitioning, the columns and rows of the matrices defined in the previous section may need to be reordered. If we consider a scattering energy E that is just slightly above the lowest scattering threshold with energy E_{th} and if we consider spin-orbit coupling parameters such that the single-minimum regime is realized, then there is one open channel and the open-open K-matrix corresponds to a 1×1 matrix. If, on the other hand, we consider the double-minimum regime with E just above E_{th} and $\tilde{\delta}=0$, then there are two open channels and the open-open K-matrix corresponds to a 2×2 matrix. Formally, we write

$$\begin{pmatrix} \underline{\Psi}_{out}^{oo} & \underline{\Psi}_{out}^{oc} \\ \underline{\Psi}_{out}^{co} & \underline{\Psi}_{out}^{cc} \end{pmatrix} = \begin{pmatrix} \underline{f}^{o} & \underline{0} \\ \underline{0} & \underline{f}^{c} \end{pmatrix} - \begin{pmatrix} \underline{g}^{o} & \underline{0} \\ \underline{0} & \underline{g}^{c} \end{pmatrix} \begin{pmatrix} \underline{K}^{oo} & \underline{K}^{oc} \\ \underline{K}^{co} & \underline{K}^{cc} \end{pmatrix}, \tag{44}$$

where the matrices with superscripts "oo", "cc", "co", and "oc" have dimensions $N^o\times N^o$, $N^c\times N^c$, $N^c\times N^o$, and $N^o\times N^c$ ($N^o+N^c=4n_{max}$).

The idea is [35–38] to construct a linear combination of the asymptotic solution, Eq. (44), so that the divergent parts are removed. Following Refs. [6, 35–38], we write the coefficient matrix that "rearranges" the asymptotic solution as $(\underline{I},\underline{Y}^{co})^T$, where $\underline{I}$ is the identity matrix of size $N^o\times N^o$. Acting with both sides of Eq. (44) onto $(\underline{I},\underline{Y}^{co})^T$, we obtain

$$\begin{pmatrix} \underline{\Psi}_{out}^{oo} + \underline{\Psi}_{out}^{oc}\underline{Y}^{co} \\ \underline{\Psi}_{out}^{co} + \underline{\Psi}_{out}^{cc}\underline{Y}^{co} \end{pmatrix} = \begin{pmatrix} \underline{f}^{o} - \underline{g}^{o}\underline{K}^{oo} & -\underline{g}^{o}\underline{K}^{oc} \\ -\underline{g}^{c}\underline{K}^{co} & \underline{f}^{c} - \underline{g}^{c}\underline{K}^{cc} \end{pmatrix} \begin{pmatrix} \underline{I} \\ \underline{Y}^{co} \end{pmatrix}. \tag{45}$$

To remove the diverging part, $\underline{Y}^{co}$ needs to satisfy

$$-\underline{g}^{c}\underline{K}^{co} + \left(\underline{f}^{c} - \underline{g}^{c}\underline{K}^{cc}\right)\underline{Y}^{co} = 0. \tag{46}$$

Solving for $\underline{Y}^{co}$ and inserting the result into the first line of Eq. (45), we find

$$\begin{aligned} &\underline{\Psi}_{out}^{oo} + \underline{\Psi}_{out}^{oc}\underline{Y}^{co} \\ &= \underline{f}^{o} - \underline{g}^{o}\underline{K}^{oo} - \underline{g}^{o}\underline{K}^{oc}\left[(\underline{g}^{c})^{-1}\underline{f}^{c} - \underline{K}^{cc}\right]^{-1}\underline{K}^{co}. \end{aligned} \tag{47}$$

Using that $(\underline{g}^{c})^{-1}\underline{f}^{c} = -\imath\underline{I}$ [6, 35–38], we obtain the final expression,

$$\underline{\Psi}_{out}^{oo} + \underline{\Psi}_{out}^{oc}\underline{Y}^{co} = \underline{f}^{o} - \underline{g}^{o}\underline{K}_{phys}, \tag{48}$$

where the physical K-matrix $\underline{K}_{phys}$ is defined as [5, 6, 38]

$$\underline{K}_{phys} = \underline{K}^{oo} + \imath\underline{K}^{oc}(\underline{I} - \imath\underline{K}^{cc})^{-1}\underline{K}^{co}. \tag{49}$$

The first term on the right hand side of Eq. (49) is the "usual" term, which describes particles entering and leaving in the open channel(s). The second term incorporates "higher-order processes", which describe particles entering in the open channel, transitioning to intermediate closed channels, and leaving in the open channel.

In addition to the K-matrix, we consider the scattering amplitude matrix $\underline{\mathcal{F}}$ (note that the scattering amplitude matrix is usually denoted by $\underline{f}$; however, we use $\underline{\mathcal{F}}$ instead since the symbol $\underline{f}$ is used to denote the regular solution). The scattering amplitude matrix $\underline{\mathcal{F}}$,

$$\underline{\mathcal{F}} = \imath\underline{K}_{phys}\left(\underline{I} - \imath\underline{K}_{phys}\right)^{-1}, \tag{50}$$

at fixed scattering energy E (the energy dependence is not indicated explicitly) defines the matrix elements $\mathcal{T}_{st}$ and $\mathcal{R}_{st}$ of the transmission coefficient matrix $\underline{\mathcal{T}}$ and the reflection coefficient matrix $\underline{\mathcal{R}}$, respectively,

$$\mathcal{T}_{st} = |\delta_{st} + \mathcal{F}_{st}|^2 \tag{51}$$

and

$$\mathcal{R}_{st} = |\mathcal{F}_{st}|^2. \tag{52}$$

In Eqs. (51)-(52), the second subscript denotes the incoming channel and the first subscript the outgoing channel. This implies that the transmission coefficient $\mathcal{T}_t$, which quantifies the fraction of transmitted flux, provided the incoming flux is located in channel t, is given by

$$\mathcal{T}_t = \sum_{s \in \text{open}} \mathcal{T}_{st}. \tag{53}$$

Similarly, the reflection coefficient $\mathcal{R}_t$, which quantifies the fraction of reflected flux, provided the incoming flux is located in channel t, is given by

$$\mathcal{R}_t = \sum_{s \in \text{open}} \mathcal{R}_{st}. \tag{54}$$

The total transmission and reflection coefficients $\mathcal{T}$ and $\mathcal{R}$ are defined by

$$\mathcal{T} = \sum_{t \in \text{open}} \mathcal{T}_t \tag{55}$$

and

$$\mathcal{R} = \sum_{t \in \text{open}} \mathcal{R}_t, \tag{56}$$

respectively. In Eqs. (53)-(56) the sum extends over the N^{o} energetically open channels. As required by flux conservation, the above definitions are consistent with the identity

$$\mathcal{T} + \mathcal{R} = N^{\text{o}}. \tag{57}$$

If $\underline{K}_{\text{phys}}$ has only one non-vanishing eigen value (denoted by $K^{(1)}_{\text{phys}}$), then $\mathcal{R}$ is given by

$$\mathcal{R} = \frac{(K^{(1)}_{\text{phys}})^2}{1 + (K^{(1)}_{\text{phys}})^2}. \tag{58}$$

IV. APPROXIMATE "ROTATION APPROACH"

This section introduces an alternative but approximate scheme, referred to as "rotation approach" [21], to obtain the scattering observables numerically. Compared to the full coupled-channel treatment, the rotation approach is numerically more efficient and does not require the implementation of a propagator customized for the treatment of systems with spin-orbit coupling (Hamiltonian that contains terms proportional to $\hat{p}_z^2$ and $\hat{p}_z$). While it is not fully clear how to estimate the accuracy of the rotation approach *a priori*, numerical tests show that it works quite accurately for a wide range of spin-orbit coupling parameters. In addition to simplifying the numerics, the rotation approach can also be used to make back-of-the-envelope type estimates of the expected resonance structure based on the knowledge of the system without spin-orbit coupling, at least for a subset of the parameter space.

Just as the full coupled-channel approach, the rotation approach divides the space along z into an inner and an outer region. The full Hamiltonian in the inner region is replaced by a rotated Hamiltonian. The rotation needs to be undone when writing out the matching condition.

The idea is to define the rotated Hamiltonian $\hat{H}^R_{\text{rel}}$ in terms of a rotation operator $\hat{R}$ [21, 22],

$$\hat{H}^R_{\text{rel}} = \hat{R}^{-1} \hat{H}_{\text{rel}} \hat{R}, \tag{59}$$

such that $\hat{H}^R_{\text{rel}}$ contains a second derivative with respect to z but not a first derivative with respect to z. Choosing (inspired by Refs. [21, 22])

$$\hat{R} = \exp(-\imath k_{\text{so}} \hat{\Sigma}_z z) \tag{60}$$

and assuming $V_{S_0}(\vec{r}) = V_{T_0}(\vec{r}) = V_0(\vec{r})$, we find

$$\hat{H}^R_{\text{rel}} = \hat{H}_{\text{ho}} + \hat{T}_{\text{rel},z} + \hat{V}_{\text{int}} + \hat{V}^R_{\text{so}}, \tag{61}$$

where

$$\begin{aligned}\hat{V}^R_{\text{so}} = &- E_{\text{so}} \hat{\Sigma}_z^2 \\ &+ \frac{\hbar\Omega}{2}\Big[\hat{\sigma}_{1,x} \otimes \hat{I}_2 \cos(k_{\text{so}} z) - \hat{\sigma}_{1,y} \otimes \hat{I}_2 \sin(k_{\text{so}} z)\Big] \\ &+ \frac{\hbar\Omega}{2}\Big[\hat{I}_1 \otimes \hat{\sigma}_{2,x} \cos(k_{\text{so}} z) - \hat{I}_1 \otimes \hat{\sigma}_{2,y} \sin(k_{\text{so}} z)\Big] \\ &+ \frac{\hbar\tilde{\delta}}{2}(\hat{\sigma}_{1,z} \otimes \hat{I}_2 + \hat{I}_1 \otimes \hat{\sigma}_{2,z}).\end{aligned} \tag{62}$$

Equations (61) and (62) show that the term linear in $\hat{p}_z$ is, indeed, absent. The simplification of the derivative terms comes "at a price", however. The rotation or gauge transformation introduces a new term [first term on the right-hand-side of Eq. (62)] as well as a spatially oscillating Raman coupling strength Ω. So far, no approximations have been made, i.e., the rotated Hamiltonian in Eq. (61) is equivalent to the original Hamiltonian $\hat{H}_{\text{rel}}$ given in Eq. (12).

Assuming that $k_{\text{so}}|z|$ is small and Taylor expanding the sin and cos terms to leading order, we find the following small-$|z|$ expression for the spin-orbit coupling term,

$$\begin{aligned}\hat{V}^{R,\text{sr}}_{\text{so}} = &- E_{\text{so}} \hat{\Sigma}_z^2 + \frac{\hbar\Omega}{2}(\hat{\sigma}_{1,x} \otimes \hat{I}_2 + \hat{I}_1 \otimes \hat{\sigma}_{2,x}) + \\ &\frac{\hbar\tilde{\delta}}{2}(\hat{\sigma}_{1,z} \otimes \hat{I}_2 + \hat{I}_1 \otimes \hat{\sigma}_{2,z}),\end{aligned} \tag{63}$$

where the superscript "sr" indicates that this expression is only valid for sufficiently small $k_{\rm so}|z|$. The next order correction is proportional to $\Omega k_{\rm so}|z|$. The premise is that the phase accumulation has reached its asymptotic value, at least to a very good approximation, before the next-order terms in the expansions of the oscillating Ω terms become important. We denote the corresponding small-$|z|$ Hamiltonian by $\hat{H}_{\rm rel}^{R,{\rm sr}}$. Since $\hat{H}_{\rm rel}^{R,{\rm sr}}$ does not contain any first derivative terms with respect to z, the corresponding Schrödinger equation can be propagated using any "standard" propagator. Denoting the resulting logarithmic derivative matrix by $\underline{\mathcal{Y}}^{R,{\rm sr}}(z)$, the approximate logarithmic derivative matrix in the singlet-triplet basis, obtained within the rotation approach, reads (see Ref. [21] for an analogous derivation)

$$\underline{\mathcal{Y}}^{\rm sr}(z) = \left(\frac{d\underline{R}(z)}{dz}\right)\,(\underline{R}(z))^{-1} + \underline{R}(z)\,\underline{\mathcal{Y}}^{R,{\rm sr}}(z)\,\,(\underline{R}(z))^{-1}\,, \qquad (64)$$

where $\underline{R}(z)$ is the matrix representation of $\hat{R}$ in the singlet-triplet basis (see Appendix C).

Expressed in the spin basis $\{|R_j\rangle\}$ (see Appendix C), $\hat{V}_{\rm so}^{R,{\rm sr}}$ is not diagonal. In the special case that the interactions in the singlet and triplet channels are all equal $[V_0(\vec{r}) = V_{T_{+1}}(\vec{r}) = V_{T_{-1}}(\vec{r})]$, $\hat{V}_{\rm so}^{R,{\rm sr}}$ can be diagonalized by applying another transformation. Defining

$$\hat{H}_{\rm rel}^{UR,{\rm sr}} = U^\dagger \hat{H}_{\rm rel}^{R,{\rm sr}} U, \qquad (65)$$

the resulting small-$|z|$ Hamiltonian $\hat{H}_{\rm rel}^{UR,{\rm sr}}$ reads

$$\hat{H}_{\rm rel}^{UR,{\rm sr}} = \hat{H}_{\rm ho} + \hat{T}_{{\rm rel},z} + \hat{V}_{\rm int} + \sum_{j=1}^{4} \epsilon_j |D_j\rangle\langle D_j|, \qquad (66)$$

where the energy shifts ϵ_j are determined by the solutions to the equation

$$\epsilon_j^4 + 2E_{\rm so}\epsilon_j^3 + (E_{\rm so}^2 - E_\Omega^2 - E_{\tilde{\delta}}^2)\epsilon_j^2 - (E_\Omega^2 + 2E_{\tilde{\delta}}^2)E_{\rm so}\epsilon_j - E_{\rm so}^2 E_{\tilde{\delta}}^2 = 0. \qquad (67)$$

For $\tilde{\delta} = 0$, one finds

$$\epsilon_1 = 0, \qquad (68)$$

$$\epsilon_2 = -E_{\rm so}, \qquad (69)$$

and

$$\epsilon_{3/4} = \frac{1}{2}\left(-E_{\rm so} \mp \sqrt{E_{\rm so}^2 + (2E_\Omega)^2}\right). \qquad (70)$$

The matrix representation $\underline{U}$ of U and the basis states $|D_j\rangle$ are given in Appendix C for $\tilde{\delta} = 0$. For what follows, it is important that the basis states $|D_1\rangle$, $|D_3\rangle$, and $|D_4\rangle$ are symmetric under the exchange of the two particles while the basis state $|D_2\rangle$ is anti-symmetric under the exchange of the two particles. Depending on the particle symmetry (BB versus FF), the combination of z- and ρ-dependent functions has to be chosen accordingly.

The approximate Hamiltonian $\hat{H}_{\rm rel}^{UR,{\rm sr}}$ [Eq. (66)] is nearly identical to the full Hamiltonian $\hat{H}_{\rm rel}$. The difference is that the term proportional to $\hat{p}_z$ in $\hat{H}_{\rm rel}$ is replaced by the channel specific energy shifts ϵ_j in $\hat{H}_{\rm rel}^{UR,{\rm sr}}$. In addition to having gotten rid of the first derivative term, the approximate Hamiltonian $\hat{H}_{\rm rel}^{UR,{\rm sr}}$ has another key characteristic: it is diagonal in the $|D_j\rangle$ basis. This implies that the propagation in the four channels labeled by $|D_j\rangle$ can be done independently, with the energy shift ϵ_j merely leading to a modified scattering energy. Thus, the approximate short-range Hamiltonian corresponds to four "standard" wave guide problems in the absence of spin-orbit coupling. Compared to the standard wave guide problem, the scattering energy is replaced by the effective scattering energies $E_j^{\rm eff} = E - \epsilon_j$. The propagation of these standard wave guide sub-systems can be accomplished using essentially any propagator.

Having separately propagated the four sub-systems of size $n_{\rm max} \times n_{\rm max}$, the logarithmic derivative matrix $\underline{\mathcal{Y}}^{UR,{\rm sr}}(z)$ of size $4n_{\rm max} \times 4n_{\rm max}$ is constructed by combining the four $n_{\rm max} \times n_{\rm max}$ logarithmic derivative matrices. As in the full coupled-channel treatment, the channels are organized such that the four $n_\rho = 0$ states are first, followed by the four $n_\rho = 1$ states, and so on. To transform from the $|D_j\rangle$ basis to the singlet-triplet basis, the rotation needs to be "undone". The resulting expression for the logarithmic derivative matrix in the singlet-triplet basis reads

$$\underline{\mathcal{Y}}^{\rm sr}(z) = \left(\frac{d\underline{R}(z)}{dz}\right)\underline{U}\,\,(\underline{R}(z)\,\underline{U})^{-1} + \underline{R}(z)\,\underline{U}\,\underline{\mathcal{Y}}^{UR,{\rm sr}}(z)\,\,(\underline{R}(z)\,\underline{U})^{-1}\,. \qquad (71)$$

Equations (64) and (71) show that there are two terms that contribute to the logarithmic derivative matrix $\underline{\mathcal{Y}}^{\rm sr}(z)$, which is expressed in the spin-orbit coupling basis (i.e., in the same asymptotic basis as that used in Sec. III). The first term on the right hand side of Eqs. (64) and (71) is due to the fact that the rotation operator $\hat{R}$ is z-dependent. The matrix $\underline{\mathcal{Y}}^{\rm sr}(z)$ couples, just as the exact logarithmic derivative matrix $\underline{\mathcal{Y}}(z)$, different states of the spin singlet-triplet basis. Having $\underline{\mathcal{Y}}^{\rm sr}(z)$, the K-matrix is obtained by replacing $\underline{\mathcal{Y}}(z)$ in Eq. (25) by $\underline{\mathcal{Y}}^{\rm sr}(z)$. We refer to the resulting K-matrix as $\underline{K}^{\rm sr}(z)$. The superscript "sr" serves to remind the reader that the K-matrix is obtained using the approximate small-$|z|$ logarithmic derivative matrix.

Importantly, the matching to the asymptotic solution in the rotation approach is done in exactly the same way as in the full coupled-channel treatment. This implies that the procedure for determining and interpreting the physical K-matrix $\underline{K}_{\rm phys}^{\rm sr}$ obtained from $\underline{K}^{\rm sr}$ is identical to that outlined in Sec. III B. The "only" approximation made in the rotation approach is how the small-$|z|$ phase is being accumulated.

To assess the validity of the rotation approach, Fig. 3

compares scaled elements of the physical K-matrix for two identical fermions with interaction in the singlet channel only obtained using the rotation approach (pluses) and the full Hamiltonian (lines). Figure 4 considers two identical fermions with identical interactions in all four channels. In both figures, the non-vanishing interactions are modeled by a Gaussian potential $V_{\rm G}(r)$,

$$V_{\rm G}(r) = v_0 \exp\left(-\frac{r^2}{2r_0^2}\right), \tag{72}$$

with range $r_0 = 0.3a_{\rm ho}/\sqrt{2}$ and varying depth v_0 ($v_0 < 0$). The scattering energy E is set to $E_{\rm th}$ and the generalized detuning $\tilde{\delta}$ to zero.

Figures 3(a) and 4(a) show the quantity $-k_z a_{\rm ho}(\underline{K}_{\rm phys}(k_z))_{11}$ (the reasoning behind this scaling is discussed in Sec. V B) for $E_\Omega = \hbar\omega/100$ (double-minimum regime) as a function of the magnitude of v_0. The agreement between the pluses and the lines indicates that the rotation approach provides a quantitatively correct description of the scattering observables in the small E_Ω regime. Figures 3(b) and 4(b) show the quantity $K_{\rm phys}(k_z)/(k_z a_{\rm ho})$ for a larger E_Ω (namely, $E_\Omega = \hbar\omega$; single-minimum regime). It can be seen that the results obtained by the rotation approach deviate visibly from the full calculation. Importantly, however, the rotation approach provides a semi-quantitatively correct description even for this large Raman coupling strength. In particular, the rotation approach reproduces the sharp resonance feature around $|v_0| = 70\hbar\omega$ in Fig. 4(b). Compared to the system with interaction in the singlet channel only, the system with equal interactions in all four channels supports a richer resonance structure. Our analysis shows that the resonances near $|v_0| = 60\hbar\omega$ in Fig. 4(a) and near $|v_0| = 60\hbar\omega$ and $|v_0| = 70\hbar\omega$ in Fig. 4(b) involve the p-wave scattering volume.

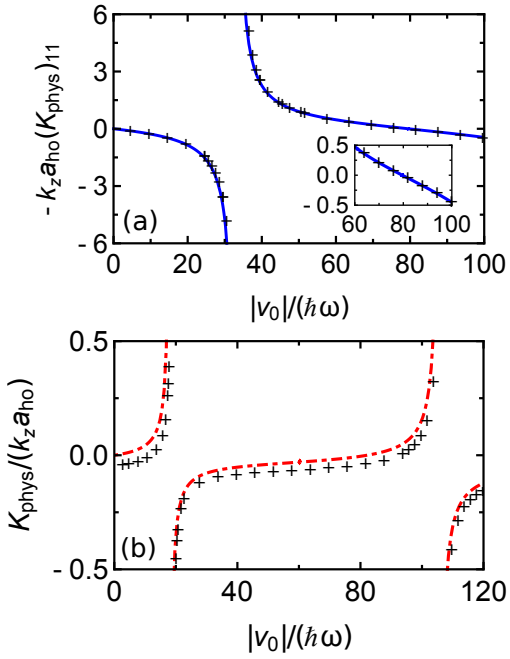

FIG. 3: (color online) Benchmarking the rotation approach. The lines and pluses show scattering results obtained from the full propagation and the rotation approach, respectively, for two identical fermions interacting through a Gaussian potential with range $r_0 = 0.3a_{\rm ho}/\sqrt{2}$ in the singlet channel only as a function of the magnitude of the depth v_0 of the potential. The results are obtained for $(k_{\rm so})^{-1} = (0.2\sqrt{2})^{-1}a_{\rm ho}$, $\tilde{\delta} = 0$, and $E = E_{\rm th}$. Panel (a) shows the quantity $-k_z a_{\rm ho}(\underline{K}_{\rm phys}(k_z))_{11}$ for $E_\Omega = \hbar\omega/100$. The inset in (a) shows a blow-up of the main panel. Panel (b) shows the quantity $K_{\rm phys}(k_z)/(k_z a_{\rm ho})$ for $E_\Omega = \hbar\omega$.

V. EFFECTIVE ONE-DIMENSIONAL COUPLING CONSTANTS

An alternative approach to determining the scattering solutions consists of calculating effective one-dimensional coupling constants by "integrating out" the $n_\rho > 0$ channels. The effective one-dimensional coupling constants, in turn, provide the input for an effective strictly one-dimensional 4×4 Hamiltonian $H_{\rm 1d}$. Assuming interactions in the singlet channel only, this approach was pursued in Refs. [19, 20]. To set the stage, Sec. V A reviews selected properties of the effective one-dimensional coupling constants in the absence of spin-orbit coupling [1, 5]. These reference results will be very useful for interpreting the results in the presence of spin-orbit coupling. Section V B discusses the effective one-dimensional 4×4 Hamiltonian and analyzes the threshold behavior in the vicinity of the lowest and higher-lying scattering thresholds.

A. Reference system: Wave guide without spin-orbit coupling terms

In the absence of spin-orbit coupling ($k_{\rm so} = \Omega = \tilde{\delta} = 0$), the four spin channels are decoupled and the problem reduces to that of two particles in a wave guide. In this case, the singlet channel is combined with an even-z spatial wave function. In the limit of zero-range interactions and a scattering energy E of $\hbar\omega$, this is the wave guide system considered in Olshanii's seminal work [1]. Non-threshold scattering energies were subsequently considered in Refs. [5, 7, 39, 40]. Each of the triplet channels is combined with an odd-z spatial wave function. In the limit of short-range interactions, this is the wave guide system considered by Granger and Blume [5]. In the presence of the spin-orbit coupling terms, neither the total spin nor the corresponding projection quantum number are conserved. As a consequence, the singlet and triplet channels are mixed and the structure of the scattering resonances may be modified compared to the scenarios without spin-orbit coupling terms.

We start our discussion with the singlet channel. In what follows, we set the quantum number m_l equal to

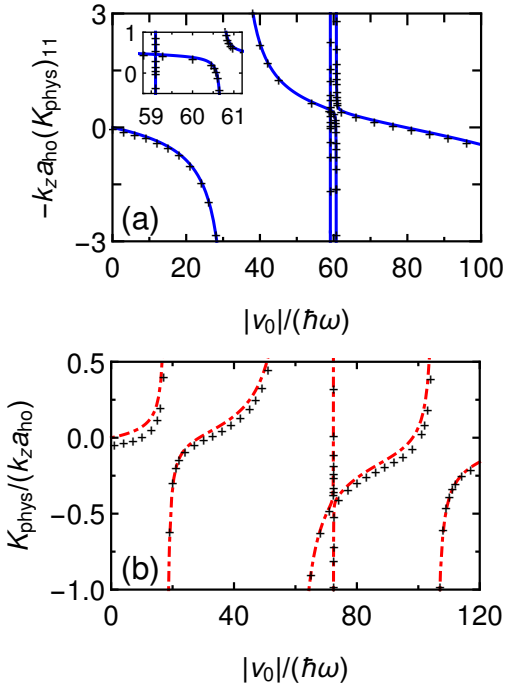

FIG. 4: (color online) Benchmarking the rotation approach. The lines and pluses show scattering results obtained from the full propagation and the rotation approach, respectively, for two identical fermions interacting through a Gaussian potentials with range $r_0 = 0.3a_{ho}/\sqrt{2}$ in all four channels as a function of the magnitude of the potential depth v_0. The results are obtained for $(k_{so})^{-1} = (0.2\sqrt{2})^{-1}a_{ho}$, $\tilde{\delta} = 0$, and $E = E_{th}$. Panel (a) shows the quantity $-k_z a_{ho}(\underline{K}_{phys}(k_z))_{11}$ for $E_\Omega = \hbar\omega/100$. The inset in (a) shows a blow-up of the main panel. Despite the enlarged scale, the resonance near $|v_0| = 59\hbar\omega$ is not fully resolved. Panel (b) shows the quantity $K_{phys}(k_z)/(k_z a_{ho})$ for $E_\Omega = \hbar\omega$.

0. Modeling the interaction in the singlet channel by a zero-range pseudo-potential characterized by the free-space s-wave scattering length a_s and enforcing that the spatial wave function is even with respect to z, the effective one-dimensional interaction potential $V_{1d}^{even}(z)$ can be parametrized in terms of the one-dimensional coupling constant $g_{1d}^{even}(k_z)$ [1, 5],

$$V_{1d}^{even}(z) = g_{1d}^{even}(k_z)\delta(z), \tag{73}$$

where $g_{1d}^{even}(k_z)$ is given by

$$\frac{g_{1d}^{even}(k_z)}{\hbar\omega a_{ho}} = \frac{2a_s(E)}{a_{ho}}\left[1 + \frac{a_s(E)}{a_{ho}}\zeta\left(\frac{1}{2}, \frac{3}{2} - \frac{E}{2\hbar\omega}\right)\right]^{-1}, \tag{74}$$

k_z denotes the scattering wave number along z,

$$E = \frac{\hbar^2 k_z^2}{2\mu} + (2n_\rho + 1)\hbar\omega, \tag{75}$$

$a_s(E)$ denotes the energy-dependent free-space s-wave scattering length, $\zeta(\cdot,\cdot)$ denotes the Hurwitz-Zeta function, and the harmonic oscillator length a_{ho} is defined in terms of the reduced mass μ,

$$a_{ho} = \sqrt{\frac{\hbar}{\mu\omega}}. \tag{76}$$

In what follows, we assume for simplicity that the scattering energy E is chosen such that the $n_\rho = 0$ channel is open while all other n_ρ channels are closed ($\hbar\omega \le E < 3\hbar\omega$). Under this assumption, the effective coupling constant $g_{1d}^{even}(k_z)$ is related to the physical K-matrix $K_{phys}^{even}(k_z)$ (this is a 1×1 matrix) via

$$g_{1d}^{even}(k_z) = -\frac{\hbar^2 k_z}{\mu} K_{phys}^{even}(k_z). \tag{77}$$

The K-matrix diverges at the critical scattering length $a_s^{cr}(E)$, where

$$\frac{a_s^{cr}(E)}{a_{ho}} = -\left[\zeta\left(\frac{1}{2}, \frac{3}{2} - \frac{E}{2\hbar\omega}\right)\right]^{-1}. \tag{78}$$

For $E = E_{th} = \hbar\omega$, Eq. (78) reduces to $a_s^{cr}(E_{th}) \approx 0.6848 a_{ho}$ [1, 5]. The resonance occurs when the scattering energy is equal to the energy of a "virtual bound state" that is supported by the closed channel ($n_\rho > 0$) Hilbert space [4]. Within the zero-range framework, the energy of the virtual bound state lies exactly $2\hbar\omega$ above the energy of the true bound state [4] (throughout this manuscript, we use the convention that true bound states, calculated using the Hilbert space spanned by the full Hamiltonian, have an energy below the lowest relative scattering threshold).

In the literature, the interaction in the triplet channel has been modeled by a p-wave zero-range pseudopotential [41–46]. Denoting the energy-dependent free-space p-wave scattering volume by $V_p(E)$ and enforcing that the spatial wave function is odd with respect to z, the effective one-dimensional interaction potential $V_{1d}^{odd}(z)$ can be parametrized in terms of the one-dimensional coupling constant $g_{1d}^{odd}(k_z)$ [41],

$$V_{1d}^{odd}(z) = g_{1d}^{odd}(k_z)\frac{\overleftarrow{\partial}}{\partial z}\delta(z)\frac{\overrightarrow{\partial}}{\partial z}, \tag{79}$$

where the first derivative operator acts to the left and the second to the right. The derivative operators are needed since the spatial wave function vanishes at $z = 0$. Note that other parameterizations of the one-dimensional pseudo-potential exist (see, e.g., Refs. [47–50]). Working in the low-energy regime where only the $n_\rho = 0$ channel is energetically open, the one-dimensional coupling constant $g_{1d}^{odd}(k_z)$ [5],

$$\frac{g_{1d}^{odd}(k_z)}{\hbar\omega a_{ho}^3} = \frac{-6V_p(E)}{a_{ho}^3}\left[1 - \frac{12V_p(E)}{a_{ho}^3}\zeta\left(-\frac{1}{2}, \frac{3}{2} - \frac{E}{2\hbar\omega}\right)\right]^{-1}, \tag{80}$$

is related to the physical K-matrix $K^{\rm odd}_{\rm phys}(k_z)$ through [5]

$$g^{\rm odd}_{\rm 1d}(k_z) = \frac{\hbar^2}{\mu k_z} K^{\rm odd}_{\rm phys}(k_z). \tag{81}$$

The physical K-matrix diverges at the critical scattering volume $V_p^{\rm cr}(E)$,

$$\frac{V_p^{\rm cr}(E)}{a_{\rm ho}^3} = \left[12\zeta\left(-\frac{1}{2}, \frac{3}{2} - \frac{E}{2\hbar\omega}\right)\right]^{-1}, \tag{82}$$

which reduces to $V_p^{\rm cr}(E_{\rm th}) \approx -0.4009 a_{\rm ho}^3$ for $E = E_{\rm th} = \hbar\omega$. According to Ref. [44], the resonance occurs—as in the even-z case—when the scattering energy is equal to the energy of a virtual bound state in the closed channel ($n_\rho > 0$) Hilbert space. Since the energy of the virtual bound state coincides with the true bound state energy at threshold [44], the emergence of the true bound state can be used to identify the resonance positions of $K^{\rm odd}_{\rm phys}(k_z)$ for $k_z = 0$. Below the lowest scattering threshold, the energy of the virtual bound state deviates from the energy of the true bound state; in particular, the energy of the virtual bound state is not, as in the even-z case, shifted up by a constant with respect to the energy of the true bound state.

Our calculations in the presence of the spin-orbit coupling terms are not performed for a zero-range interaction potential but for the Gaussian interaction potential $V_{\rm G}(r)$ [see Eq. (72)]. The solid line in Fig. 5(a) and the dashed line in Fig. 5(b) show the scaled physical K-matrices $-k_z a_{\rm ho} K^{\rm even}_{\rm phys}(k_z)$ and $K^{\rm odd}_{\rm phys}(k_z)/(k_z a_{\rm ho})$, respectively, in the $k_z \to 0$ limit as a function of the magnitude of the depth v_0 of the Gaussian interaction potential with range $r_0 = 0.3 a_{\rm ho}/\sqrt{2}$. For comparison, the open circles in Fig. 5(a) show the zero-range result for the scaled K-matrix $-k_z a_{\rm ho} K^{\rm even}_{\rm phys}(k_z)$, which is obtained by using Eqs. (74) and (77) with $a_s(\hbar\omega)$; this quantity coincides with $g^{\rm even}_{\rm 1d}/(\hbar\omega a_{\rm ho})$. Similarly, the open circles in Fig. 5(b) show the zero-range result for the scaled K-matrix $K^{\rm odd}_{\rm phys}(k_z)/(k_z a_{\rm ho})$, which is obtained by using Eqs. (80) and (81) with $V_p(\hbar\omega)$; this quantity coincides with $g^{\rm odd}_{\rm 1d}/(\hbar\omega a_{\rm ho}^3)$. For the relatively large range r_0 of the Gaussian interaction potential considered, the inclusion of the energy dependence of the s-wave scattering length and p-wave scattering volume is crucial [see insets of Figs. 5(a) and 5(b)] [43, 51].

The solid and dashed lines in Fig. 5(c) show the relative energy of, respectively, the even-z and odd-z bound states for the Gaussian potential. The two-body system in a wave guide is bound if the relative energy is smaller than $\hbar\omega$. Compared to the free-space case, where the system is bound when the relative energy is smaller than zero, the wave guide leads to an enhancement of the binding of the most weakly-bound state. For example, the wave guide supports a weakly-bound even-z state for $|v_0|$ greater than zero while the system without a wave guide supports a weakly-bound s-wave state for $|v_0|$ greater than $14.91\hbar\omega$. Similarly, the wave guide supports a weakly-bound odd-z state for $|v_0|$ greater than $59.24\hbar\omega$ while the system without a wave guide supports a weakly-bound p-wave state for $|v_0|$ greater than $67.22\hbar\omega$.

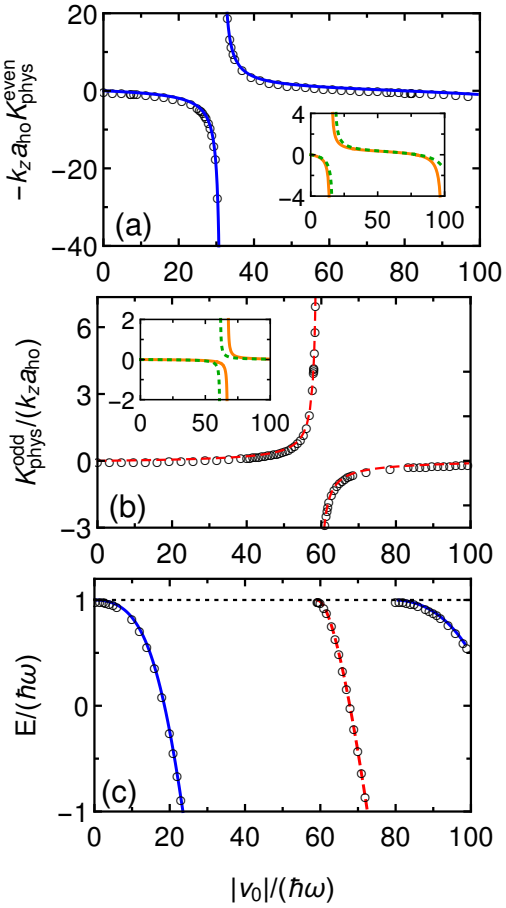

FIG. 5: (color online) Wave guide properties in the absence of spin-orbit coupling as a function of the magnitude of the depth v_0 of the Gaussian potential with $r_0 = 0.3 a_{\rm ho}/\sqrt{2}$. (a) $\lim_{k_z\to 0}[-k_z a_{\rm ho} K^{\rm even}_{\rm phys}(k_z)]$. The solid line shows finite-range results. The open circles show zero-range results that are obtained by taking the energy-dependence of the free-space scattering quantities into account. The solid and dotted lines in the inset of panel (a) show $a_s(0)/a_{\rm ho}$ and $a_s(\hbar\omega)/a_{\rm ho}$, respectively, as a function of $|v_0|/(\hbar\omega)$. (b) $\lim_{k_z\to 0}[K^{\rm odd}_{\rm phys}(k_z)/(k_z a_{\rm ho})]$. The dashed line shows finite-range results. The open circles show zero-range results that are obtained by taking the energy-dependence of the free-space scattering quantities into account. The solid and dotted lines in the inset of panel (b) show $V_p(0)/a_{\rm ho}^3$ and $V_p(\hbar\omega)/a_{\rm ho}^3$, respectively, as a function of $|v_0|/(\hbar\omega)$. (c) Relative energy of the even-z (solid lines) and odd-z (dashed line) bound states for the finite-range potential. The open circles show the zero-range results. To aid the readability, the horizontal dashed line indicates the threshold energy $E_{\rm th}$.

For comparison, the open circles in Fig. 5(c) show the zero-range results, which are obtained by solving the zero-range eigen energy equations self-consistently, accounting for the energy-dependence of the s-wave scat-

tering length and p-wave scattering volume [52]. The agreement between the zero-range and finite-range binding energies is quite good on the scale shown, demonstrating that the zero-range treatment provides a reliable description even though the range of our two-body Gaussian potential is quite large. We note, however, that the extremely small finite-range binding energies near $|v_0| \approx 80\hbar\omega$ and near $|v_0| \approx 60\hbar\omega$ are not well reproduced by the zero-range models. The reason is that the quantities a_s/r_0 and $|V_p|^{1/3}/r_0$, respectively, are not notably smaller than one for these $|v_0|$.

Figure 5 serves as a reference for the calculations presented in Sec. VI, which account for the spin-orbit coupling terms. In particular, that section explores how the resonances shift as a function of the spin-orbit coupling parameters.

B. Effective one-dimensional 4×4 low-energy Hamiltonian

Assuming s-wave zero-range interactions (modeled using the three-dimensional Fermi-Huang pseudopotential) in the singlet channel only and setting m_l to zero, Refs. [19, 20] derived the following effective strictly one-dimensional Hamiltonian $H_{1\mathrm{d}}$ in the relative coordinate z for two identical fermions,

$$H_{1\mathrm{d}} = \left(-\frac{\hbar^2}{2\mu}\frac{\partial^2}{\partial z^2} + \hbar\omega\right)\hat{I}_1 \otimes \hat{I}_2 + \hat{V}_{\mathrm{so}} + g_{1\mathrm{d}}^{\mathrm{soc}}(k_z)\delta(z)|S_0\rangle\langle S_0|. \quad (83)$$

The quantity $\hat{V}_{\mathrm{so}}$ is defined in Eq. (15) and the one-dimensional coupling constant $g_{1\mathrm{d}}^{\mathrm{soc}}(k_z)$ results from "integrating out" the $n_\rho > 0$ harmonic oscillator channels. If the scattering energy E is chosen such that only a subset of the four $n_\rho = 0$ channels is open, then $g_{1\mathrm{d}}^{\mathrm{soc}}$ corresponds to an "unphysical effective coupling constant". The "physical effective coupling constant" is obtained by eliminating the energetically closed $n_\rho = 0$ channels from $\underline{K}_{1\mathrm{d}}$ (see below). Importantly, $\underline{K}_{1\mathrm{d}}$ is derived from a three-dimensional Hamiltonian; the "1d" subscript is used to distinguish the zero-range treatment (Refs. [19, 20]) from the finite-range treatment discussed in the previous sections. We emphasize that the derivation of the effective one-dimensional Hamiltonian given in Eq. (83) assumes that all $n_\rho > 0$ channels are energetically closed [19, 20]. This restricts the scattering energy to values $E < E_{\mathrm{th}} + 2\hbar\omega$. For certain relatively large E_Ω or E_{so}, the scattering energy may be further restricted due to a "reordering" of the non-interacting relative dispersion curves (i.e., the minimum of a dispersion curve with $n_\rho = 0$ may lie above the minimum of a dispersion curve with $n_\rho = 1$). This is discussed further in Sec. VI B.

For $\tilde{\delta} = 0$, Ref. [19] writes $g_{1\mathrm{d}}^{\mathrm{soc}}$ as (see the last two equations before the reference section)

$$\frac{g_{1\mathrm{d}}^{\mathrm{soc}}}{\hbar\omega a_{\mathrm{ho}}} = \frac{2a_s}{a_{\mathrm{ho}}}\left[1 + \frac{a_s}{a_{\mathrm{ho}}}C\left(\frac{E}{\hbar\omega}, \frac{E_\Omega}{\hbar\omega}, \frac{E_{\mathrm{so}}}{\hbar\omega}\right)\right]^{-1} \quad (84)$$

with

$$C\left(\frac{E}{\hbar\omega}, \frac{E_\Omega}{\hbar\omega}, \frac{E_{\mathrm{so}}}{\hbar\omega}\right) = -C_1\left(\frac{E}{\hbar\omega}\right) - C_2\left(\frac{E}{\hbar\omega}, \frac{E_\Omega}{\hbar\omega}, \frac{E_{\mathrm{so}}}{\hbar\omega}\right), \quad (85)$$

where the functions C_1 and C_2 are given in terms of one- and two-dimensional integrals, respectively. Equation (84) has the same functional form as Eq. (74), except that the Hurwitz-Zeta function is replaced by the three-parameter function C. Taylor-expanding the function C about $E_\Omega/(\hbar\omega) = 0$, we find

$$C\left(\frac{E}{\hbar\omega}, \frac{E_\Omega}{\hbar\omega}, \frac{E_{\mathrm{so}}}{\hbar\omega}\right) \approx D_0\left(\frac{E + E_{\mathrm{so}}}{\hbar\omega}\right) + D_1\left(\frac{E}{\hbar\omega}, \frac{E_{\mathrm{so}}}{\hbar\omega}, \frac{E_\Omega}{\hbar\omega}\right) + \mathcal{O}\left(\frac{E_\Omega^4}{(\hbar\omega)^4}\right), \quad (86)$$

where

$$D_0\left(\frac{E + E_{\mathrm{so}}}{\hbar\omega}\right) = \zeta\left(\frac{1}{2}, \frac{3}{2} - \frac{(E + E_{\mathrm{so}})}{2\hbar\omega}\right) \quad (87)$$

and

$$D_1\left(\frac{E}{\hbar\omega}, \frac{E_{\mathrm{so}}}{\hbar\omega}, \frac{E_\Omega}{\hbar\omega}\right) = -\frac{E_\Omega^2}{(\hbar\omega)^2}\left(\frac{E_{\mathrm{so}}}{\hbar\omega}\right)^{-1} \times \left[\frac{1}{8}\zeta\left(\frac{3}{2}, \frac{3}{2} - \frac{E}{2\hbar\omega}\right) - \frac{1}{8}\zeta\left(\frac{3}{2}, \frac{3}{2} - \frac{E + E_{\mathrm{so}}}{2\hbar\omega}\right) + \sum_{n=0}^{\infty}\frac{1}{4\sqrt{\pi}n!(2n+1)}\left(\frac{E_{\mathrm{so}}}{2\hbar\omega}\right)^{n+1}\Gamma\left(n + \frac{5}{2}\right) \times \zeta\left(n + \frac{5}{2}, \frac{3}{2} - \frac{E}{2\hbar\omega}\right)\right]. \quad (88)$$

The sum over n on the right hand side of Eq. (88) converges relatively quickly. Figures 6(a) and 6(b) show the fractional differences $(C - D_0)/C$ and $(C - D_0 - D_1)/C$, respectively, for $E = E_{\mathrm{th}}$. It can be seen that the fractional difference $(C - D_0)/C$ is smaller than about 30% for the ranges of $E_\Omega/(\hbar\omega)$ and $E_{\mathrm{so}}/(\hbar\omega)$ considered. Moreover, Fig. 6(b) demonstrates that the approximation provides a description at an accuracy of 2% or better for a wide range of parameter combinations. This suggests that the approximate but compact expansion can be used over a fairly large parameter space unless high accuracy results are sought.

The Taylor expansion given in Eq. (86) can be understood from the analysis presented in Sec. IV. To see this we consider the small-$|z|$ Hamiltonian $\hat{H}_{\mathrm{rel}}^{UR,\mathrm{sr}}$ [Eq. (66)], which is diagonal in the $|D_j\rangle$ basis. The derivation of $\hat{H}_{\mathrm{rel}}^{UR,\mathrm{sr}}$ assumed that the interactions in all four channels are equal. It may thus seem that we cannot apply it to the case with interaction in the singlet channel

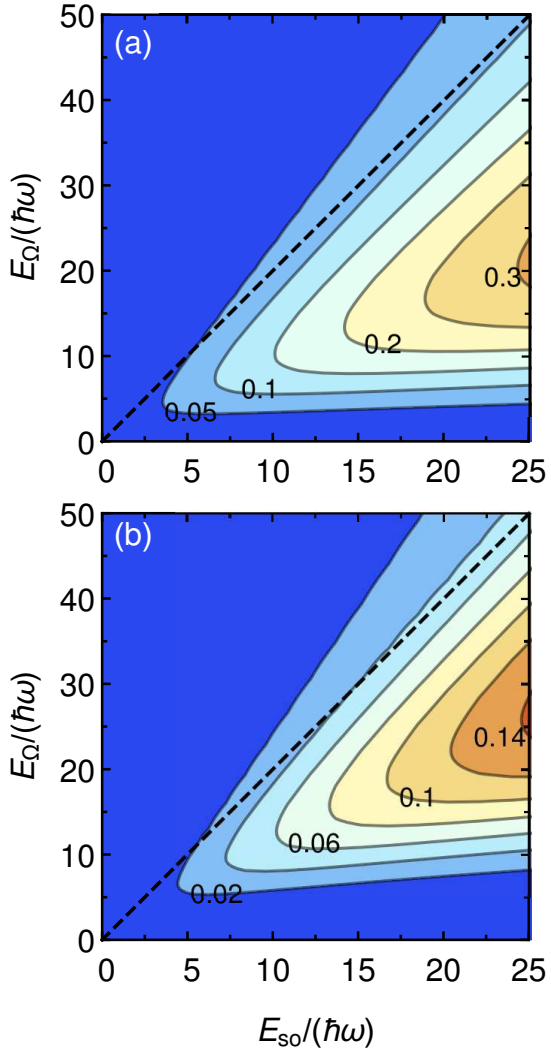

FIG. 6: (color online) Benchmarking the accuracy of the Taylor expansion given in Eq. (86), which provides a simple approximate means to evaluate the effective one-dimensional coupling constant $g_{\rm 1d}^{\rm soc}$. Panels (a) and (b) show contour plots of the fractional differences $(C-D_0)/C$ and $(C-D_0-D_1)/C$, respectively, as functions of $E_\Omega/(\hbar\omega)$ and $E_{\rm so}/(\hbar\omega)$ for $E = E_{\rm th}$. The contours are spaced equidistantly (selected contours are labeled). The dashed lines mark the transition from the double-minimum to the single-minimum regime.

only considered here. However, if we add the Fermi-Huang pseudo-potential to the three triplet channels, the zero-range results summarized above remain unaltered since the Fermi-Huang pseudo-potential only acts when the spatial wave function component is non-zero at $\vec{r}=0$. This implies that the Hamiltonian $\hat{H}_{\rm rel}^{UR,{\rm sr}}$ applies to the case considered here. Combining the energy shift $\epsilon_2 = -E_{\rm so}$ in the anti-symmetric $|D_2\rangle$ channel with the scattering energy E [see Eqs. (66) and (69)], the phase shift that is being accumulated in the $|D_2\rangle$ channel is the same as the one that would be accumulated in the absence of the spin-orbit coupling terms for the energy $E+E_{\rm so}$ as opposed to for E. This explains why $g_{\rm 1d}^{\rm soc}$ in Eq. (84) has, approximately, the same functional form as in the absence of spin-orbit coupling, except that the scattering energy is replaced by the effective scattering energy $E+E_{\rm so}$. Correspondingly, the higher-order corrections in the Taylor expansion in Eq. (86) can be interpreted as representing the correction terms that would arise in the rotation approach if higher-order terms in $k_{\rm so}|z|$ were taken into account in Eq. (66).

When Eq. (84) is applied to predict or to reproduce results for finite-range potentials, the energy-dependence of a_s should be taken into account. Section VI evaluates the scattering length a_s that enters into $g_{\rm 1d}^{\rm soc}(k_z)$ [see Eq. (84)] at the scattering energy E.

Section VI compares the physical K-matrix $\underline{K}_{\rm phys}$ for finite-range interactions, obtained using the formalism discussed in Sec. III, with the physical K-matrix $\underline{K}_{\rm 1d,phys}$ obtained by determining the scattering solutions for the effective one-dimensional Hamiltonian. In what follows, we restrict our discussion to the $\tilde{\delta}=0$ case. The 4×4 K-matrix $\underline{K}_{\rm 1d}$ for the strictly one-dimensional Hamiltonian can be readily obtained analytically in terms of $g_{\rm 1d}^{\rm soc}(k_z)$, E, and the spin-orbit coupling parameters. Due to their lengthy-ness, the expressions are not reproduced here. Eliminating the energetically closed channels, the physical K-matrix $\underline{K}_{\rm 1d,phys}$ can be obtained for the double-minimum and single-minimum regimes.

To illustrate the impact of the modified single-particle dispersion curves on the scattering properties, we analyze the behavior of $\underline{K}_{\rm 1d,phys}$ in the limit that the scattering energy E approaches the energy E_α, where α is equal to I, II, II', III, or IV (see the caption of Fig. 1 for the definition of E_α). For $\alpha = I$ and II (E_I and E_{II} are the threshold energies in the double-minimum and single-minimum regimes, respectively), we consider the $E\to(E_\alpha)^+$ limit. For the other α, we consider the $E\to(E_\alpha)^+$ and $E\to(E_\alpha)^-$ limits. Using the quantities $\bar{k}_\alpha^{(\pm)}$,

$$\bar{k}_\alpha^{(\pm)} = \left(\pm\frac{m}{\hbar^2}(E-E_\alpha)\right)^{1/2}, \qquad (89)$$

as small parameters, the near-threshold behavior of the physical K-matrix $\underline{K}_{\rm 1d,phys}$ and its eigenvalues $K_{\rm 1d,phys}^{(j)}$ is summarized in Table I. Note that the $\bar{k}_\alpha^{(\pm)}$ are defined as real, positive quantities, with the superscripts "(+)" and "(−)" referring to the $E\to(E_\alpha)^+$ and $E\to(E_\alpha)^-$ limits. The coefficients $a_{\alpha,s}^{(\pm)}$, $b_{\alpha,s}^{(\pm)}$, and $c_{\alpha,s}^{(\pm)}$ are determined by $g_{\rm 1d}^{\rm soc}$, $a_{\rm ho}$, $\hbar\omega$, E_Ω, and $E_{\rm so}$. In general, the analytic expressions for $a_{\alpha,s}^{(\pm)}$, $b_{\alpha,s}^{(\pm)}$, and $c_{\alpha,s}^{(\pm)}$ are quite involved. As examples, we consider $a_{I,-1}^{(+)}$ and $a_{II,1}^{(+)}$, which can both be written in the form (the functional form for the other coefficients may be different)

$$a_{\alpha,s}^{(\pm)} = A_{\alpha,s}^{(\pm)}\frac{g_{\rm 1d}^{\rm soc}}{a_{\rm ho}\hbar\omega}\left(1+\frac{g_{\rm 1d}^{\rm soc}}{a_{\rm ho}\hbar\omega}B_{\alpha,s}^{(\pm)}\right)^{-1} \qquad (90)$$

	$\underline{K}_{\rm 1d,phys}$	$K^{(j)}_{\rm 1d,phys}$
$E\to(E_I)^+$	$\begin{pmatrix} a^{(+)}_{I,-1}(\bar{k}^{(+)}_I)^{-1}+a^{(+)}_{I,0} & -a^{(+)}_{I,-1}(\bar{k}^{(+)}_I)^{-1} \\ -a^{(+)}_{I,-1}(\bar{k}^{(+)}_I)^{-1} & a^{(+)}_{I,-1}(\bar{k}^{(+)}_I)^{-1}-a^{(+)}_{I,0}\end{pmatrix}$	$j=1: 2a^{(+)}_{I,-1}(\bar{k}^{(+)}_I)^{-1}$ $j=2:0$
$E\to(E_{II})^+$	$a^{(+)}_{II,1}\bar{k}^{(+)}_{II}+a^{(+)}_{II,3}(\bar{k}^{(+)}_{II})^3$	
$E\to(E_{II'})^+$	$a_{II',0}+a^{(+)}_{II',1}\bar{k}^{(+)}_{II'}$	
$E\to(E_{II'})^-$	$\begin{pmatrix} a_{II',0} & a^{(-)}_{II',1/2}(\bar{k}^{(-)}_{II'})^{1/2} \\ a^{(-)}_{II',1/2}(\bar{k}^{(-)}_{II'})^{1/2} & a^{(-)}_{II',1}\bar{k}^{(-)}_{II'}\end{pmatrix}$	$j=1: a_{II',0}+a^{(-)}_{II',1}\bar{k}^{(-)}_{II'}$ $j=2:0$
$E\to(E_{III})^+$	$\begin{pmatrix} a^{(+)}_{III,0} & 0 & a^{(+)}_{III,-1/2}(\bar{k}^{(+)}_{III})^{-1/2} \\ 0 & 0 & 0 \\ a^{(+)}_{III,-1/2}(\bar{k}^{(+)}_{III})^{-1/2} & 0 & a^{(+)}_{III,-1}(\bar{k}^{(+)}_{III})^{-1}+a^{(+)}_{III,1}\bar{k}^{(+)}_{III}\end{pmatrix}$	$j=1: a^{(+)}_{III,-1}(\bar{k}^{(+)}_{III})^{-1}+a^{(+)}_{III,0}$ $j=2:0$ $j=3:0$
$E\to(E_{III})^-$	$a^{(-)}_{III,1}\bar{k}^{(-)}_{III}+a^{(-)}_{III,2}(\bar{k}^{(-)}_{III})^2$	
$E\to(E_{IV})^+$	$\begin{pmatrix} a_{IV,0} & 0 & b^{(+)}_{IV,0} & a^{(+)}_{IV,1/2}(\bar{k}^{(+)}_{IV})^{1/2} \\ 0 & 0 & 0 & 0 \\ b^{(+)}_{IV,0} & 0 & c_{IV,0} & b^{(+)}_{IV,1/2}(\bar{k}^{(+)}_{IV})^{1/2} \\ a^{(+)}_{IV,1/2}(\bar{k}^{(+)}_{IV})^{1/2} & 0 & b^{(+)}_{IV,1/2}(\bar{k}^{(+)}_{IV})^{1/2} & a^{(+)}_{IV,1}\bar{k}^{(+)}_{IV}\end{pmatrix}$	$j=1: (a_{IV,0}+c_{IV,0})+a^{(+)}_{IV,1}\bar{k}^{(+)}_{IV}$ $j=2:0$ $j=3:0$ $j=4:0$
$E\to(E_{IV})^-$	$\begin{pmatrix} a_{IV,0}+a^{(-)}_{IV,1}\bar{k}^{(-)}_{IV} & 0 & b^{(-)}_{IV,0}+b^{(-)}_{IV,1}\bar{k}^{(-)}_{IV} \\ 0 & 0 & 0 \\ b^{(-)}_{IV,0}+b^{(-)}_{IV,1}\bar{k}^{(-)}_{IV} & 0 & c_{IV,0}+c^{(-)}_{IV,1}\bar{k}^{(-)}_{IV}\end{pmatrix}$	$j=1: (a_{IV,0}+c_{IV,0})+(a^{(-)}_{IV,1}+c^{(-)}_{IV,1})\bar{k}^{(-)}_{IV}$ $j=2:0$ $j=3:0$

TABLE I: Summary of threshold laws for two identical fermions with $\tilde{\delta}=0$ obtained by analyzing the zero-range model with interaction in the singlet channel only. In the cases where $\underline{K}_{\rm 1d,phys}$ is a 1×1 matrix, the eigen value $K^{(1)}_{\rm 1d,phys}$ is not retyped in the $K^{(j)}_{\rm 1d,phys}$ column. The energies E_α, where α takes the Roman letters I, II, II', III, and IV, are defined in the caption of Fig. 1. The quantities $a^{(\pm)}_{\alpha,s}$, $b^{(\pm)}_{\alpha,s}$, and $c^{(\pm)}_{\alpha,s}$ are constants that depend on E_Ω, $E_{\rm so}$, $\hbar\omega$, $a_{\rm ho}$, and $g^{\rm soc}_{\rm 1d}$ (they are independent of E). The subscript s indicates the power of $\bar{k}^{(\pm)}_\alpha$ that the coefficient is associated with. Note the following identities: $a^{(+)}_{II',0}=a^{(-)}_{II',0}=a_{II',0}$, $a^{(+)}_{IV,0}=a^{(-)}_{IV,0}=a_{IV,0}$, and $c^{(+)}_{IV,0}=c^{(-)}_{IV,0}=c_{IV,0}$. The eigenvalues $K^{(j)}_{\rm 1d,phys}$ with $j>1$ vanish identically for all energies, not just in the vicinity of the thresholds.

with

$$A^{(+)}_{I,-1}=-\frac{\left[(2E_{\rm so})^2-E_\Omega^2\right]^{1/2}}{4a_{\rm ho}E_{\rm so}}, \tag{91}$$

$$B^{(+)}_{I,-1}=-\frac{E_\Omega^2(\hbar\omega)^{1/2}}{(2E_{\rm so})^{3/2}\left[(2E_{\rm so})^2+E_\Omega^2\right]^{1/2}}, \tag{92}$$

$$A^{(+)}_{II,1}=\frac{a_{\rm ho}\hbar\omega}{\left(E_\Omega^2-2E_{\rm so}E_\Omega\right)^{1/2}}\frac{E_{\rm so}(4E_{\rm so}-E_\Omega)}{(E_\Omega^2-6E_{\rm so}E_\Omega+8E_{\rm so}^2)}, \tag{93}$$

and

$$B^{(+)}_{II,1}=\frac{\sqrt{\hbar\omega}\left[E_\Omega^{3/2}-2E_{\rm so}E_\Omega^{1/2}-2\sqrt{2}E_{\rm so}\left(E_\Omega-2E_{\rm so}\right)^{1/2}\right]}{\sqrt{2}(E_\Omega^2-6E_{\rm so}E_\Omega+8E_{\rm so}^2)}. \tag{94}$$

The coefficients $-2\hbar^2a^{(+)}_{I,-1}/\mu$ and $\hbar^2a^{(+)}_{II,1}/\mu$ can be interpreted as effective even- and odd-z coupling constants. This interpretation is motivated by the fact that the associated non-zero eigen values $K^{(1)}_{\rm 1d,phys}$ (see Table I) scale in the same way as Eqs. (81) and (77), respectively. While not pursued in this work, the effective even-z coupling constant $-2\hbar^2a^{(+)}_{I,-1}/\mu$ and the effective odd-z coupling constant $\hbar^2a^{(+)}_{II,1}/\mu$ should provide the starting point for developing an effective low-energy single-band description of the system. We note that the threshold behavior and structure of the coefficients can also, with quite a bit of work, be deduced from the results presented in the *Method Section* of Ref. [19].

Inspection of Table I shows that the eigen value $K^{(1)}_{\rm 1d,phys}$ has the characteristics of the usual odd-z threshold behavior in the vicinity of $(E_{II})^+$ and $(E_{III})^-$ and the usual even-z threshold behavior in the vicinity of $(E_I)^+$ and $(E_{III})^+$. In the vicinity of $(E_{II'})^\pm$ and $(E_{IV})^\pm$, the threshold behavior of the eigen value $K^{(1)}_{\rm 1d,phys}$ is unusual (no energy dependence). This demonstrates the non-trivial impact of the spin-orbit coupling terms in the low-energy regime. We note that some of the matrix elements of the physical K-matrix near the scattering thresholds contain half-integer powers of the small wave vector $\bar{k}^{(\pm)}_\alpha$. Since the scaling with $\bar{k}^{(\pm)}_\alpha$ changes across some of the higher-lying scattering thresholds, Table I suggests that the scattering observables across some scattering thresholds may not be smooth. This will be elaborated on further in Sec. VI B. A "jump" in the total reflection coefficient across one of the scattering thresholds was already pointed out in the context of Fig. 2 of Ref. [19].

VI. SCATTERING OBSERVABLES FOR TWO IDENTICAL FERMIONS WITH INTERACTION IN THE SINGLET CHANNEL

This section considers the effect of the spin-orbit coupling terms on the scattering observables for two identical fermions with interaction in the singlet channel only for $\tilde{\delta} = 0$ and a $(k_{\rm so})^{-1}$ that is much larger than the transverse confinement length $a_{\rm ho}$, namely $(k_{\rm so})^{-1} \approx 3.54 a_{\rm ho}$. Various Raman coupling strengths Ω and potential depths v_0 are considered. A naive expectation might be that a small $k_{\rm so}$ can only weakly perturb the scattering properties obtained in the absence of spin-orbit coupling. This section shows that this naive expectation is not necessarily correct, i.e., the spin-orbit coupling terms can induce significant changes even for $(k_{\rm so})^{-1} \gg a_{\rm ho}$.

For two identical fermions, the $|T_0\rangle$ channel experiences, in general, the same interaction as the $|S_0\rangle$ channel. The interaction in the $|T_0\rangle$ channel does, however, not lead to any appreciable scattering for short-range interactions tuned away from free-space p-wave resonances, implying that the interaction in the $|T_0\rangle$ channel can be set to zero for most parameter combinations without noticeable changes. Section VI A considers scattering properties at the threshold ($E = E_{\rm th}$) while Sec. VI B considers the above threshold behavior ($E > E_{\rm th}$).

A. Scattering properties at the lowest scattering threshold

This section compares our finite-range results for $\underline{K}_{\rm phys}$ and its eigenvalues $K^{(j)}_{\rm phys}$ with the physical K-matrix $\underline{K}_{\rm 1d,phys}$ and its eigenvalues $K^{(j)}_{\rm 1d,phys}$, which are obtained, as discussed in Sec. V B, by using $g^{\rm soc}_{\rm 1d}(k_z)$ as input. We emphasize that the energy dependence of $g^{\rm soc}_{\rm 1d}$, via the energy dependence of the s-wave scattering length and the function C [see Eq. (84)], needs to be accounted for when comparing the results.

We start our discussion by considering the double-minimum regime. The lines in Fig. 7 show the eigenvalues $K^{(j)}_{\rm phys}$ of $\underline{K}_{\rm phys}$ as a function of the absolute value of the depth v_0 of the two-body Gaussian potential with range $r_0 = 0.3 a_{\rm ho}/\sqrt{2}$ for various Ω. Motivated by the threshold law for the zero-range interactions (see Table I), Fig. 7(a) shows the quantity $\lim_{k_z\to 0}[-k_z a_{\rm ho} K^{(1)}_{\rm phys}(k_z)]$, which can be interpreted as an *effective* (dimensionless) even-parity coupling constant. For $E_\Omega \ll E_{\rm so}$, the four spin channels are approximately decoupled and the $k_{\rm so}$ term can, in a lowest-order treatment, be gauged away. As a consequence, the system properties are, to leading order, expected to be identical to those obtained for the wave guide in the absence of spin-orbit coupling but with s-wave interactions. The solid line in Fig. 7(a) shows the scaled eigen value for $E_\Omega = \hbar\omega/100 = E_{\rm so}/4$. For this small E_Ω, the scaled eigen value $-k_z a_{\rm ho} K^{(1)}_{\rm phys}(k_z)$ is approximately equal to $g^{\rm even}_{\rm 1d}/(\hbar\omega a_{\rm ho})$ [(dimensionless) even-parity coupling constant in the absence of spin-orbit coupling, Eq. (77) with $a_s(E_{\rm th})$; see open circles in Fig. 7(a)]. This confirms that $-(\hbar^2 k_z/\mu) K^{(1)}_{\rm phys}(k_z)$ behaves, at least in this small-E_Ω limit, like an effective one-dimensional even-parity coupling constant and that the system in the $E_\Omega \to 0$ limit deviates only weakly from the system without spin-orbit coupling. Figure 7(a) shows that the divergence of $-k_z a_{\rm ho} K^{(1)}_{\rm phys}(k_z)$ moves to larger $|v_0|$ [corresponding to smaller $a_s(E_{\rm th})$] as E_Ω increases from $0.25 E_{\rm so}$ (solid line) to $0.75 E_{\rm so}$ (dashed line) to $1.5 E_{\rm so}$ (dotted line) to $1.975 E_{\rm so}$ (dash-dotted line). At the same time, the resonance becomes—this can be seen when the data in Fig. 7(a) are replotted as a function of the scattering length—narrower. We attribute the narrowing of the resonances with increasing E_Ω to the fact that the contribution of the $|S_0\rangle$ channel to the lowest threshold decreases with increasing E_Ω. The results for the finite-range potential [lines in Fig. 7(a)] are well reproduced by the results for the zero-range model that accounts for the spin-orbit coupling [filled circles in Fig. 7(a)].

The zero-range model predicts that the second eigenvalue of $\underline{K}_{\rm 1d,phys}(k_z)$ vanishes identically in the double-minimum regime for all energies (see Table I). In constrast, $K^{(2)}_{\rm phys}(k_z)$ does not vanish for the finite-range interaction potential. Specifically, we find that $K^{(2)}_{\rm phys}(k_z)/(k_z a_{\rm ho})$ approaches a constant in the small k_z limit [see lines in Fig. 7(b)]. This scaling suggests that the quantity $\lim_{k_z\to 0}[\hbar^2/(\mu k_z) K^{(2)}_{\rm phys}(k_z)]$ can be interpreted as an *effective* odd-z coupling constant. To elucidate this interpretation, we focus on the well depth v_0, at which $K^{(2)}_{\rm phys}(k_z)/(k_z a_{\rm ho})$ diverges ($|v_0| \approx 80\hbar\omega$). Comparison with Fig. 5(c) shows that $K^{(2)}_{\rm phys}(k_z)/(k_z a_{\rm ho})$ diverges at approximately the same v_0 at which the system with-

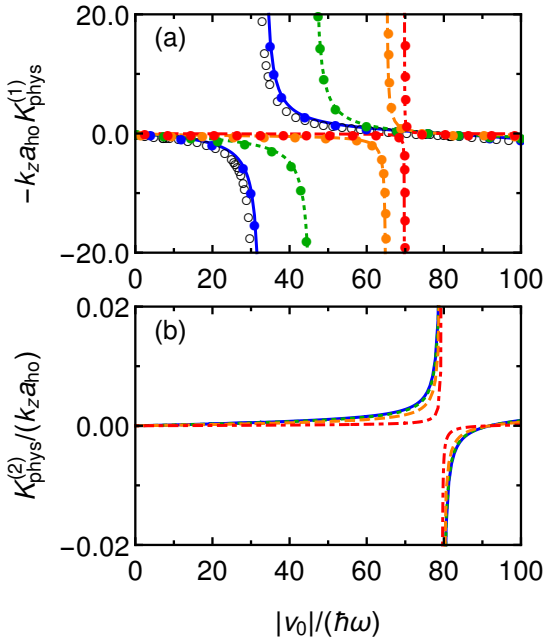

FIG. 7: (color online) Scattering properties for two identical fermions in the presence of spin-orbit coupling with interaction in the singlet channel only for $r_0 = 0.3a_{\rm ho}/\sqrt{2}$, $(k_{\rm so})^{-1} = (0.2\sqrt{2})^{-1}a_{\rm ho}$, and $\tilde{\delta} = 0$ (double-minimum regime). Lines show the scaled eigenvalues (a) $\lim_{k_z\to 0}[-k_z a_{\rm ho} K^{(1)}_{\rm phys}(k_z)]$ and (b) $\lim_{k_z\to 0}[K^{(2)}_{\rm phys}(k_z)/(k_z a_{\rm ho})]$, obtained by diagonalizing the physical 2×2 K-matrix $\underline{K}_{\rm phys}(k_z)$, as a function of the magnitude of the depth v_0 of the Gaussian interaction potential. Blue solid, green dotted, orange dashed, and red dash-dotted lines are for $E_\Omega = 0.01\hbar\omega$, $0.03\hbar\omega$, $0.06\hbar\omega$, and $0.079\hbar\omega$ (corresponding to $E_\Omega = 0.25E_{\rm so}, 0.75E_{\rm so}, 1.5E_{\rm so}$, and $1.975E_{\rm so}$), respectively. In panel (a), the open circles show the even-z zero-range coupling constant $g^{\rm even}_{\rm 1d}(k_z = 0)$ [Eq. (77); spin-orbit coupling effects are not accounted for] and the filled circles show the quantity $\lim_{k_z\to 0}[-k_z a_{\rm ho} K^{(1)}_{\rm 1d,phys}(k_z)]$.

out spin-orbit coupling supports an even-z bound state with infinitesimally small binding energy. To calculate the bound state energies in the presence of the spin-orbit coupling terms and the external wave guide confinement, we employ a basis set expansion approach [33, 53]. Our results (see lines in Fig. 8) show that the critical v_0, at which a new two-body bound state is first supported for the $k_{\rm so}$ considered ($\Omega < \Omega_*$), does not differ significantly from the case without spin-orbit coupling. We find that the bound state in the presence of spin-orbit coupling contains, in general, both even- and odd-z contributions. For $\Omega < \Omega_*$, the triplet contribution is largest when the binding energy is smallest. Correspondingly, the effective odd-z coupling constant $[\hbar^2/(\mu k_z)]K^{(2)}_{\rm phys}(k_z)$ diverges when a new bound state is being pulled in. For comparison, the filled circles in Fig. 8 show the energy of the bound state predicted by the zero-range calculations in the presence of spin-orbit coupling [Eq. (27) of Ref. [20]]. The agreement with our finite-range calculations is good, confirming the validity of both the finite- and zero-range bound state calculations. We find that the width of the resonance feature in Fig. 7(b) decreases with decreasing r_0, suggesting that the finiteness of $K^{(2)}_{\rm phys}(k_z)/(k_z a_{\rm ho})$ is, indeed, due to the finite range of the Gaussian interaction potential.

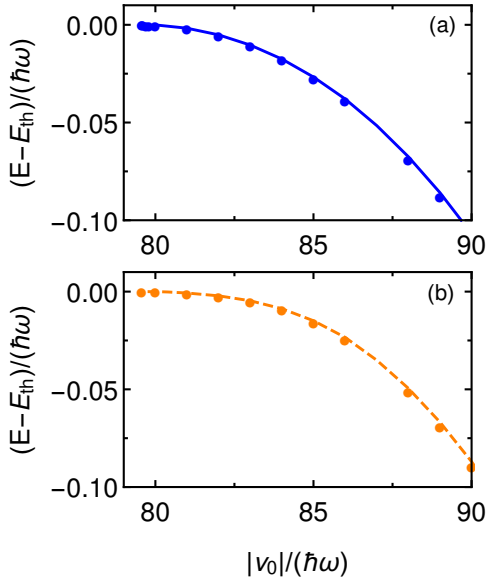

FIG. 8: (color online) Bound state properties for two identical fermions in the presence of spin-orbit coupling with interaction in the singlet channel only for $r_0 = 0.3a_{\rm ho}/\sqrt{2}$, $(k_{\rm so})^{-1} = (0.2\sqrt{2})^{-1}a_{\rm ho}$, and $\tilde{\delta} = 0$ (double-minimum regime). The solid lines show the energy of the bound state, relative to the lowest scattering threshold, as a function of the magnitude of the depth v_0 for (a) $E_\Omega = \hbar\omega/100 = E_{\rm so}/4$ and (b) $E_\Omega = 3\hbar\omega/50 = 3E_{\rm so}/2$. For comparison, the filled circles show the zero-range energies, relative to the lowest scattering threshold, obtained by solving the eigen equation in the presence of spin-orbit coupling self-consistently [see Eq. (27) of Ref. [20]].

The physical K-matrix contains, in general, off-diagonal matrix elements, which reflect the fact that the different spin channels are coupled and correspondingly that there exists a coupling between the even-l and odd-l partial wave channels due to the presence of the spin-orbit coupling terms. Diagonalizing the physical K-matrix, as done to obtain the results shown in Fig. 7, corresponds to changing the asymptotic basis that the inner solution is being matched to. While such a basis transformation provides—as illustrated above—useful insights, we emphasize that the full physical K-matrix $\underline{K}_{\rm phys}(k_z)$ is needed to determine, e.g., partial transmission and reflection coefficients.

For $E_\Omega \gg E_{\rm so}$ (single-minimum regime), one can apply a rotation to the relative Hamiltonian such that it is approximately block-diagonal. Since the lowest scattering threshold for $\Omega > \Omega_*$ has only triplet contributions and since the interactions in the triplet channels are set

to zero in this section, one naively expects that scattering resonances would be absent. However, since there exists a coupling between the different channels, the existence of a bound state due to the interaction in the $|S_0\rangle$ channel leads, as discussed next, to a scattering resonance, provided the scattering energy is degenerate with the bound state energy (see also Ref. [19]).

Motivated by the threshold laws reported in Table I, the dash-dotted line in Fig. 9 shows the scaled physical K-matrix $\lim_{k_z\to 0}[K_{\rm phys}(k_z)/(k_z a_{\rm ho})]$ for $E_\Omega = 25E_{\rm so} = \hbar\omega$ as a function of the magnitude of the depth v_0 of the two-body potential with $r_0 = 0.3a_{\rm ho}/\sqrt{2}$. The results are in good agreement with the zero-range model predictions (filled circles in Fig. 9). The dash-dotted line in Fig. 9 diverges at $|v_0| = 105.7\hbar\omega$. Figure 10(b) shows that this is the same v_0 at which the bound state becomes unbound (the dash-dotted line shows the energy of the bound state, relative to the energy of the lowest threshold, for the same parameters). The energy of the bound state is reproduced reasonably well by solving the eigen equation that does not account for the spin-orbit coupling terms self-consistently for the even-z zero-range energy, using the energy-dependent s-wave scattering length [open circles in Fig. 10(b)]. Even though the bound state becomes, strictly speaking, unbound when its energy is above $E_{\rm th}$, we can think of the bound state as turning into a resonance or quasi-bound state for $E > E_{\rm th}$. The resonance state, in turn, becomes unbound when it hits the minimum of the second-lowest dispersion curve (recall that one of the two degenerate states associated with this second-lowest scattering threshold is a pure $|S_0\rangle$ state), which sits E_Ω above $E_{\rm th}$ (here, $E_\Omega = \hbar\omega$). While we did not calculate the energy of this resonance state for the finite-range Gaussian potential, we believe that the open circles shown in Fig. 10(b) provide a reasonable description of the energy of the resonance state. As discussed further in Sec. VI B (see also Ref. [19]), the resonance state leads to an above-threshold scattering resonance (reflection coefficient of one in Fig. 15). For comparison, the filled circles in Fig. 10(b) show the energy of the bound state predicted by Eq. (27) of Ref. [20] for the zero-range interaction model in the presence of spin-orbit coupling (again, the equation is solved self-consistently). The agreement with the dash-dotted line is reasonably good.

Figure 9 shows that the resonance position shifts with decreasing Ω. Importantly, the resonance position coincides with the position where the energy of the bound state in the presence of the spin-orbit coupling terms hits the lowest scattering threshold for all $\Omega > \Omega_*$. Since the deviations from the block-diagonal structure of the rotated Hamiltonian increase with decreasing Ω, the resonance becomes broader (the broadness of the resonance is measured in terms of the width in the scattering length; the corresponding plot is not shown). This interpretation is consistent with our analysis of the bound state wave function for an energy just below the scattering threshold. For $E_\Omega = 25E_{\rm so}$ and $E_\Omega = 2.025E_{\rm so}$, e.g., the bound

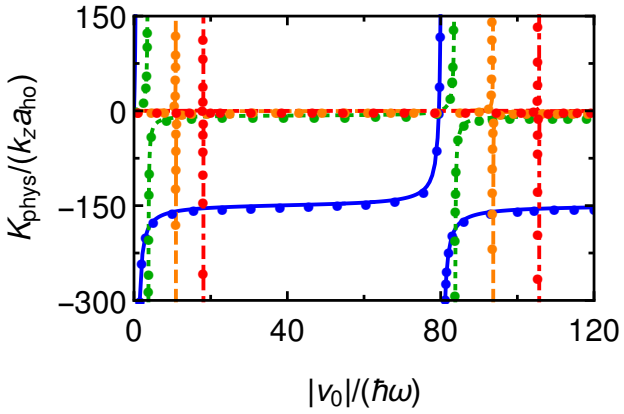

FIG. 9: (color online) Scattering properties for two identical fermions in the presence of spin-orbit coupling with interaction in the singlet channel only for $r_0 = 0.3a_{\rm ho}/\sqrt{2}$, $(k_{\rm so})^{-1} = (0.2\sqrt{2})^{-1}a_{\rm ho}$, and $\tilde{\delta} = 0$ (single-minimum regime). Blue solid, green dotted, orange dashed, and red dash-dotted lines show the scaled physical K-matrix $\lim_{k_z\to 0}[K_{\rm phys}(k_z)/(k_z a_{\rm ho})]$ as a function of the magnitude of the depth v_0 of the Gaussian potential for $E_\Omega = 2.025E_{\rm so}$, $2.5E_{\rm so}$, $7.5E_{\rm so}$, and $25E_{\rm so}$, respectively. The filled circles show the quantity $\lim_{k_z\to 0}[K_{\rm 1d,phys}(k_z)/(k_z a_{\rm ho})]$.

state with binding energy $1.14\times 10^{-4}\hbar\omega$ has a probability of about 21 % and 5 %, respectively, to be in the $|S_0\rangle$ channel. Moreover, since the coupling between the different spin channels increases with decreasing Ω, the bound state energy is, for smaller Ω, not overly well reproduced by the bound state expression that does not account for the spin-orbit coupling [open circles in Fig. 10(a)]. As expected, the bound state energy is well reproduced by the zero-range expression from Ref. [20] [filled circles in Fig. 10(a)], provided the energy-dependence of the scattering length is accounted for.

Figure 9 shows another interesting aspect. Close to the transition from the single-minimum to the double-minimum regime (the solid line is for $E_\Omega = 2.025E_{\rm so}$), the quantity $K_{\rm phys}(k_z)/(k_z a_{\rm ho})$ is negative and approximately constant for all v_0 away from the resonance. This behavior is in agreement with the zero-range results. Taylor expanding the coefficient $a^{(+)}_{II,1}$ [see Eqs. (90), (93), and (94)], which governs the near-threshold behavior of $K_{\rm 1d,phys}$ in the single-minimum regime, around $\Omega = \Omega_*$, we find

$$(a_{\rm ho})^{-1}a^{(+)}_{II,1} = -\frac{E_{\rm so}}{E_\Omega - 2E_{\rm so}}\frac{1}{k_{\rm so}a_{\rm ho}}. \qquad (95)$$

Correspondingly, the quantity $\lim_{k_z\to 0} K_{\rm 1d,phys}(k_z)/(k_z a_{\rm ho})$ approaches negative infinity for all interaction strengths when Ω approaches Ω_* from above. The fact that the scaled K-matrix goes to minus infinity regardless of the details of the underlying two-body potential indicates that the physics is governed by the relative dispersion curves. As Ω approaches Ω_*, the bottom of the relative dispersion

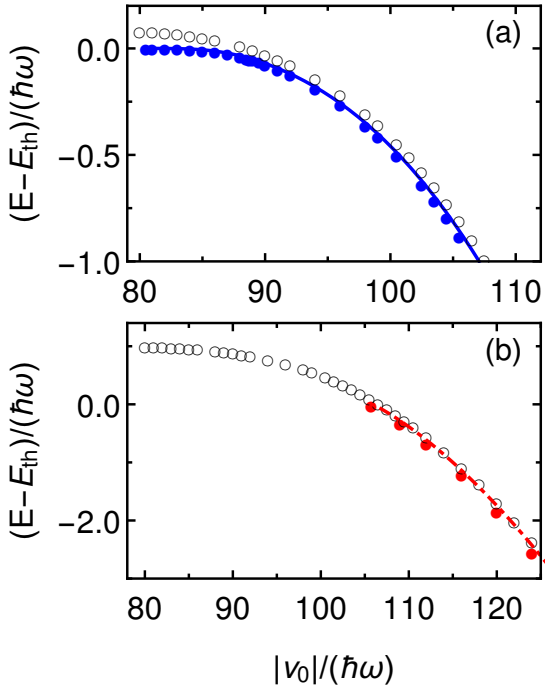

FIG. 10: (color online) Bound state energies for two identical fermions in the presence of spin-orbit coupling with interaction in the singlet channel only for $r_0 = 0.3a_{\rm ho}/\sqrt{2}$, $(k_{\rm so})^{-1} = (0.2\sqrt{2})^{-1}a_{\rm ho}$, and $\tilde{\delta} = 0$ (single-minimum regime). Solid and dash-dotted lines show the energy of the bound state, relative to the lowest scattering threshold, as a function of the magnitude of the depth v_0 of the Gaussian potential for (a) $E_\Omega = 2.025E_{\rm so}$ and (b) $E_\Omega = 25E_{\rm so}$, respectively. The filled circles and open circles show the energy of the zero-range model in the presence and absence of spin-orbit coupling terms; the zero-range eigen energy equations are solved self-consistently, taking the energy-dependence of the s-wave scattering length into account.

curve becomes "flatter", thereby leading to a larger density of states or degeneracy. In terms of the Bose-Fermi duality [54, 55], one can interpret the fact that the effective odd-z coupling constant goes to infinity as a signature of bosonization, which is facilitated by the enhanced degeneracy [56].

Figure 11 shows the energy-dependent s-wave scattering length $a_s(E_{\rm th})$ at which the divergence for the scattering energy $E = E_{\rm th}$ and $(k_{\rm so})^{-1} = (0.2\sqrt{2})^{-1}a_{\rm ho}$ occurs as a function of Ω. The resonance positions are calculated for the Gaussian potential with a relatively large range r_0, namely $r_0 = 0.3a_{\rm ho}/\sqrt{2}$. Repeating the calculations in selected cases for smaller r_0, we find that the resonance occurs at roughly the same s-wave scattering length, provided the energy-dependent scattering lengths $a_s(E_{\rm th})$ for two different potentials are compared. The solid, dotted, and dashed lines show the resonance positions of $k_z a_{\rm ho}\underline{K}_{\rm phys}$ $(\Omega < \Omega_*)$, $K^{(2)}_{\rm phys}/(k_z a_{\rm ho})$ $(\Omega < \Omega_*)$, and $K_{\rm phys}/(k_z a_{\rm ho})$ $(\Omega > \Omega_*)$, respectively. The zero-range predictions (filled circles) agree well with the results for the finite-range potential. It can be seen that the resonance position can be tuned significantly by the spin-orbit coupling terms.

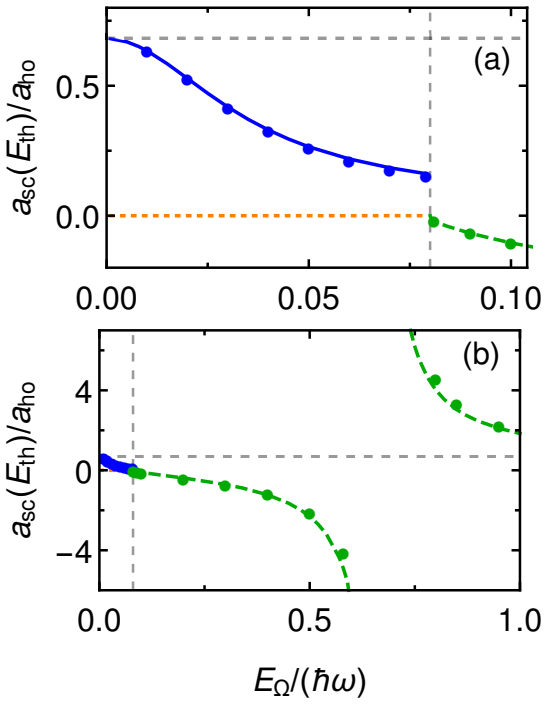

FIG. 11: (color online) Summary of resonance positions for two identical fermions with interaction in the singlet channel only. The blue solid, orange dotted, and green dashed lines show the resonance positions, obtained for the Gaussian interaction model, of $\lim_{k_z\to 0}[k_z a_{\rm ho}\underline{K}_{\rm phys}(k_z)]$ in the double-minimum regime, $\lim_{k_z\to 0}[k_z a_{\rm ho}K^{(2)}_{\rm phys}(k_z)]$ in the double-minimum regime, and $\lim_{k_z\to 0}[K_{\rm phys}(k_z)/(k_z a_{\rm ho})]$ in the single-minimum regime, respectively. For comparison, the filled circles show the zero-range results, which are obtained by taking the energy-dependence of $g^{\rm soc}_{\rm 1d}$ into account. Panels (a) and (b) cover different E_Ω ranges. The grey dashed horizontal line marks the resonance position for the case where spin-orbit coupling is absent (even-z solution). The grey dashed vertical line marks the transition from the double-minimum to the single-minimum regime.

B. Scattering properties as a function of the energy

This section extends the calculations presented in the previous section to scattering energies above the scattering threshold. As in the previous section, we keep the transverse confinement length $a_{\rm ho}$ and the spin-orbit coupling strength $k_{\rm so}$ fixed and vary the Raman coupling strength Ω and the depth v_0 of the two-body potential [or, equivalently, the zero-energy s-wave scattering length $a_s(0)$]. Since the dimension of $\underline{K}_{\rm phys}$ depends on the scattering energy (the number of energetically open channels increases with increasing energy, respectively, mono-

tonically and non-monotonically in the single-minimum and double-minimum regimes), it is not convenient to present the individual K-matrix elements. Instead, we present the total reflection coefficient $\mathcal{R}$, which is obtained by combining the individual K-matrix elements [see Eqs. (50), (52), (54), and (56)]. From a physical point of view, $\mathcal{R}$ tells one the fraction of the incoming flux that is reflected, provided the incoming flux populates the energetically open channels equally. In selected cases, we discuss the decomposition of the total reflection coefficient into the coefficients $\mathcal{R}_t$, which are calculated assuming that the incoming flux populates only the t-th channel.

The dash-dotted lines and filled circles in Figs. 12(a)-12(d) show the total reflection coefficient $\mathcal{R}$ as a function of the scattering energy E for $a_s(E=0) \approx 0.612 a_{\rm ho}$ (corresponding to $r_0 = 0.3a_{\rm ho}/\sqrt{2}$ and $|v_0| = 30\hbar\omega$) and $\Omega = 0.06\hbar\omega = 1.5E_{\rm so}$ (double-minimum regime). The agreement between the dash-dotted lines, which are obtained using $\underline{K}_{\rm phys}$ for the finite-range Gaussian potential, and the green filled circles, which are obtained using the effective one-dimensional low-energy Hamiltonian $H_{\rm 1d}$ (taking the energy-dependence of the scattering length for the Gaussian potential into account), is very good. This indicates that the effective one-dimensional low-energy Hamiltonian provides a good description in this parameter regime, provided the energy-dependence of the s-wave scattering length is accounted for. The scattering energies at which the number of energetically open channels changes are shown by thin vertical lines. It can be seen that the total reflection coefficient or its derivative change discontinuously at these scattering energies. The behavior of the total reflection coefficient $\mathcal{R}$ near these scattering energies can be obtained in analytical form using the threshold behavior of the K-matrix elements listed in Table I. For example, using the results from Table I in Eq. (58), one can analytically describe the behavior of $\mathcal{R}$ near $E = E_{III} = \hbar\omega$ for $a_s \neq 0$. We find that $\mathcal{R}$ scales as $(k_{III}^{(-)})^2$ as the scattering energy approaches $\hbar\omega$ from below [this explains why $\mathcal{R}$ goes to zero as E approaches $(E_{III})^-$ in Fig. 12(b)] and that $\mathcal{R}$ goes to one [left edge of Fig. 12(c)] as the scattering energy approaches $(E_{III})^+$. The jump of $\mathcal{R}$ from zero to one at $E = E_{III} = \hbar\omega$ can be attributed to the opening of new channels as the energy changes from below $\hbar\omega$ to above $\hbar\omega$. The behavior of the total reflection coefficient $\mathcal{R}$ just below $E = 2.9375\hbar\omega$ is a bit different. As E approaches $2.9375\hbar\omega$ from below, the reflection coefficient does not go to zero but takes a value that depends on the system parameters. For the case at hand, the close-to-zero value of $\mathcal{R}$ just below $E = 2.9375\hbar\omega$ can be traced back to the suppression of $\mathcal{R}$ by a small $g_{\rm 1d}^{\rm soc}$.

The dashed, dotted, and solid lines in Fig. 12 show the coefficients $\mathcal{R}_1$, $\mathcal{R}_3$, and $\mathcal{R}_4$. The sum of these coefficients, including only the energetically open channels, yields $\mathcal{R}$. It can be seen that the total reflection coefficient $\mathcal{R}$ contains appreciable contributions from multiple coefficients $\mathcal{R}_t$ in the cases where more than one channel is energetically open [Figs. 12(a), 12(c), and 12(d)]. The reason that multiple $\mathcal{R}_t$ contribute is a consequence of the fact that the spin-orbit coupling terms in the double-minimum regime induce, in general, a non-perturbative coupling between the singlet and triplet spin states. As discussed in Sec. III B, the sum of $\mathcal{R}$ and $\mathcal{T}$ is equal to the number $N^{\rm o}$ of energetically open channels, i.e., equal to 2, 1, 3, and 4 for Figs. 12(a), 12(b), 12(c), and 12(d), respectively. Thus, the system is "fully transparent" for scattering energies $E \lesssim \hbar\omega$, "nearly fully transparent" for $E \lesssim 2.9375\hbar\omega$ (see above), and "fully reflective" for a scattering energy a bit larger than $0.94\hbar\omega$ (but not for $E = E_{\rm th}$).

To understand the dependence of the total reflection coefficient on the scattering length, we analyze $\underline{K}_{\rm 1d,phys}$, obtained from the effective low-energy Hamiltonian for the zero-range potential, for the same $k_{\rm so}$ and Ω as those considered in Fig. 12. Figures 13(a)-13(d) show contour plots of the reflection coefficient $\mathcal{R}$ as functions of the s-wave scattering length a_s and the scattering energy E [the energy regions considered are the same as in Figs. 12(a)-12(d)]. The reflection coefficient shows an appreciable scattering length dependence. Interestingly, the reflection coefficient $\mathcal{R}$ approaches one at the lowest scattering threshold for all s-wave scattering lengths, except for $a_s = 0$. This is analogous to the situation without spin-orbit coupling (see Fig. 1 of Ref. [1]), with the difference that the total transmission coefficient $\mathcal{T}$ is also equal to one in the spin-orbit coupling case (recall, we are considering the regime where $N^{\rm o} = 2$) while it is zero in the absense of spin-orbit coupling (in this case, $N^{\rm o} = 1$). If one prepared the system in such a way that initially only the rotated state corresponding to the eigen value $K_{\rm phys,1d}^{(1)}$ was occupied, one should observe "true" full reflection. While this situation might be challenging to realize experimentally, considerations like this one help to understand the implications of the results shown in Figs. 12 and 13. As already discussed above, the two-fermion system becomes fully transparent ($\mathcal{R} = 0$) at the right edge of Fig. 13(b) and nearly fully transparent at the right edge of Fig. 13(d) for almost all s-wave scattering lengths.

We now turn to the single-minimum regime. Figures 14 and 15 mirror Figs. 12 and 13 using $E_\Omega = 1.2\hbar\omega = 30E_{\rm so}$ instead of $E_\Omega = 0.06\hbar\omega = 1.5E_{\rm so}$. Because of the large Ω, the highest relative non-interacting dispersion curve with $n_\rho = 0$ lies above the lowest relative non-interacting dispersion curve with $n_\rho = 1$ [see Fig. 14(c)]. Since the coupling constant $g_{\rm 1d}^{\rm soc}$, Eq. (84), is derived assuming that all $n_\rho \geq 1$ channels are closed, the effective one-dimensional low-energy Hamiltonian $H_{\rm 1d}$ is only valid for $E_{\rm th} \leq E \leq 1.8\hbar\omega$ even though the scattering threshold of the highest $n_\rho = 0$ channel lies at an energy of $2.2\hbar\omega$. Correspondingly, results for the effective low-energy Hamiltonian are only

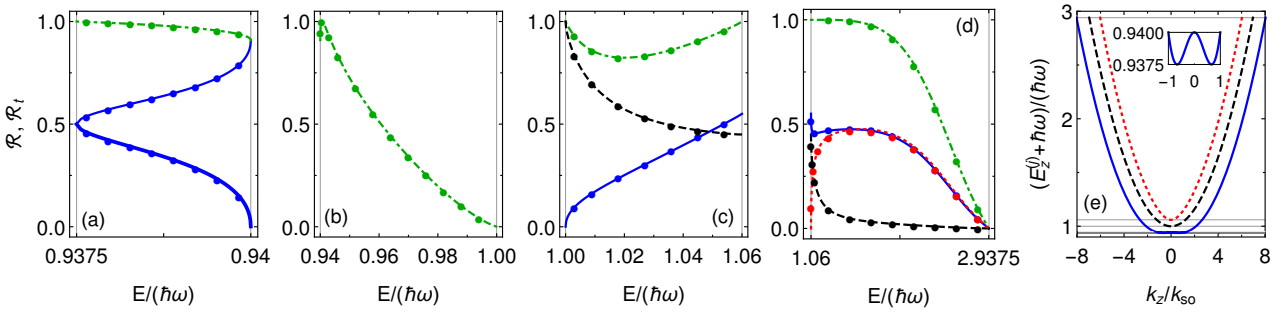

FIG. 12: (color online) Scattering observables for two identical fermions with interaction in the singlet channel only as a function of the scattering energy E for $(k_{so})^{-1} = (0.2\sqrt{2})^{-1} a_{ho}$ and $E_\Omega = 0.06\hbar\omega = 1.5E_{so}$ (double-minimum regime). The number of energetically open channels is two in panel (a), one in panel (b), three in panel (c), and four in panel (d). The green dash-dotted lines show the total reflection coefficient $\mathcal{R}$ obtained by applying the full K-matrix formalism to the Gausssian potential with $r_0 = 0.3a_{ho}/\sqrt{2}$ and $|v_0| = 30\hbar\omega$ [$a_s(0) \approx 0.612a_{ho}$]. For comparison, the filled circles show $\mathcal{R}$ obtained by using the effective one-dimensional low-energy Hamiltonian H_{1d} (the effective coupling constant g_{1d}^{soc} is determined using the energy-dependence of a_s for the Gaussian potential). The black dashed, red dotted, thin blue solid, and thick blue solid lines show the quantities $\mathcal{R}_1$, $\mathcal{R}_3$, $\mathcal{R}_{4,+}$ (solution for positive k_z), and $\mathcal{R}_{4,-}$ (solution for negative k_z), respectively, obtained using the full K-matrix formalism. $\mathcal{R}_2$ (not shown) is identically zero. The filled circles (same color coding) are obtained by using H_{1d}. The energies at which the number of energetically open scattering channels change are shown by thin vertical lines. Panel (e) shows the corresponding non-interacting relative dispersion curves. The energies at which the number of energetically open channels changes are marked by solid horizontal lines. The inset shows an enlargement of the lowest dispersion curve.

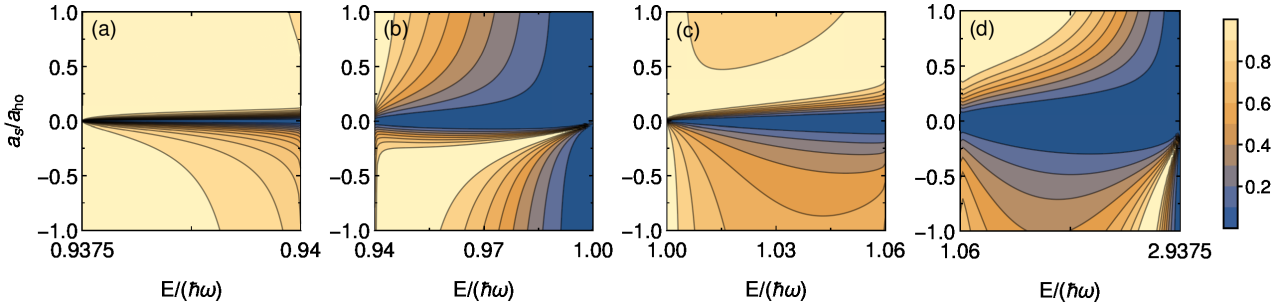

FIG. 13: (color online) Contour plot showing the total reflection coefficient $\mathcal{R}$ for two identical fermions with interactions in the singlet channel only as functions of the s-wave scattering length a_s and the scattering energy E for $(k_{so})^{-1} = (0.2\sqrt{2})^{-1} a_{ho}$ and $E_\Omega = 0.06\hbar\omega = 1.5E_{so}$ (double-minimum regime). The results are obtained using the one-dimensional effective low-energy Hamiltonian H_{1d} (a_s is treated as an input parameter).

shown in Fig. 14(a) and not in Fig. 14(b). As expected, the dash-dotted line and the filled circles in Fig. 14(a) agree well. Unlike in the double-minimum regime discussed in Fig. 12, the total reflection coefficient $\mathcal{R}$ shown in Fig. 14 is dominated by a single channel, namely by $\mathcal{R}_1$.

Interestingly, in the regime where only one channel is energetically open [Fig. 14(a), $E \leq \hbar\omega$], the system is nearly fully transparent. This can be intuitively understood by realizing that the singlet channel contribution to the lowest scattering threshold vanishes (see Fig. 2). Figure 15, which shows the total reflection coefficient $\mathcal{R}$—obtained using H_{1d}—as functions of a_s and E, confirms this. The total reflection coefficient is zero or close to zero for nearly all scattering lengths, provided the scattering energy lies between $E_{II} = -0.2\hbar\omega$ and $E_{III} = \hbar\omega$ [as already discussed above in the context of the double-minimum case, $\mathcal{R}$ approaches one as $E \to (E_{III})^-$, provided a_s is not equal to 0]. The total reflection coefficient in Fig. 14 approaches one for specific a_s. At these a_s, the system supports a resonance state (see Sec. VI A). When the scattering energy is equal to the energy of the resonance state, the incoming flux gets reflected [19].

VII. CONCLUSIONS

This paper formulated the K-matrix scattering theory for two particles in effectively one-dimensional space, realized by a tight wave guide confinement, in the presence of one-dimensional spin-orbit coupling terms and applied it to two identical fermions. The results for finite-range

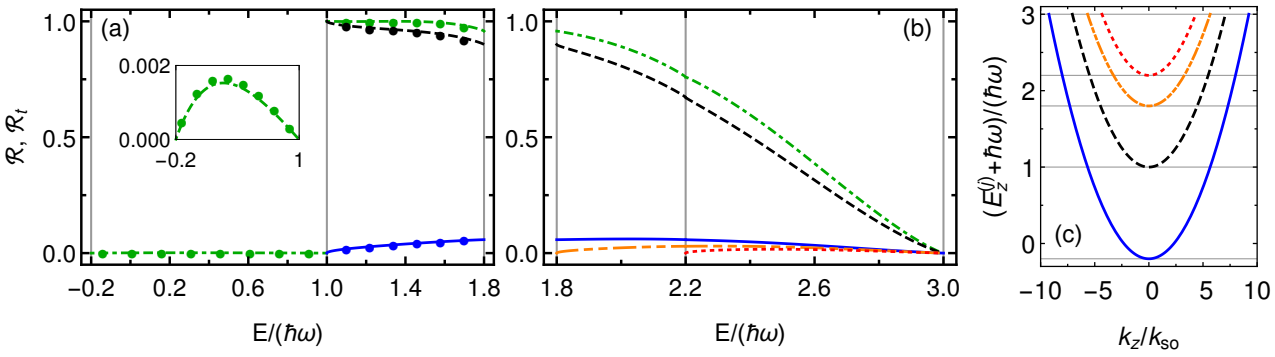

FIG. 14: (color online) Scattering observables for two identical fermions with interactions in the singlet channel only as a function of the scattering energy E for $(k_{so})^{-1} = (0.2\sqrt{2})^{-1}a_{ho}$ and $\Omega = 1.2\hbar\omega = 30E_{so}$ (single-minimum regime). The green dot-dashed lines show the total reflection coefficient $\mathcal{R}$ obtained by applying the full K-matrix formalism to the Gaussian potential with $r_0 = 0.3a_{ho}/\sqrt{2}$ and $|v_0| = 30\hbar\omega$ [$a_s(0) \approx 0.612a_{ho}$]. The black dashed, red dotted, and blue solid lines show the quantities $\mathcal{R}_1$, $\mathcal{R}_3$, and $\mathcal{R}_4$, respectively, obtained using the full K-matrix formalism. $\mathcal{R}_2$ (not shown) is identically zero. The orange dash-dot-dotted line shows the contribution to the total reflection coefficient that comes from flux entering in the lowest relative dispersion curve with $n_\rho = 1$. For comparison, the filled circles in panel (a) show the corresponding results obtained using $\underline{K}_{\text{phys,1d}}$; the effective coupling constant g_{1d}^{soc} is obtained using the energy-dependence of a_s for the Gaussian potential. The energy regime covered in panel (b) is beyond the applicability regime of the effective low-energy Hamiltonian. The thin vertical lines mark the energies at which the number of energetically open channels changes. The inset in panel (a) shows the same data as the main panel, but on an enlarged scale. Panel (c) shows the corresponding non-interacting relative dispersion curves. The blue solid, black dashed, and red dotted lines are for $n_\rho = 0$ while the dash-dot-dotted line is for $n_\rho = 1$. The energies at which the number of energetically open channels changes are marked by horizontal solid lines.

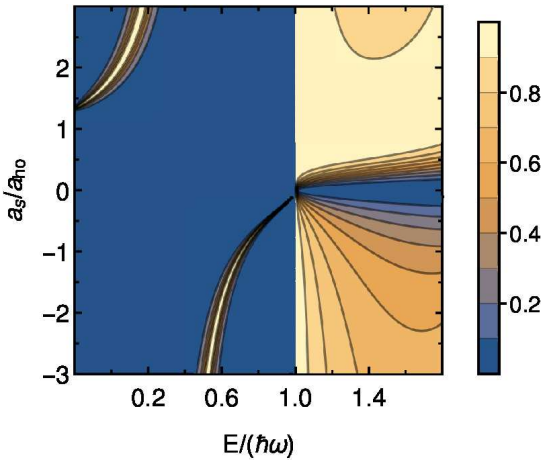

FIG. 15: (color online) Contour plot of total reflection coefficient $\mathcal{R}$ for two identical fermions with interaction in the singlet channel only as functions of the s-wave scattering length a_s and the scattering energy E for $(k_{so})^{-1} = (0.2\sqrt{2})^{-1}a_{ho}$ and $\Omega = 1.2\hbar\omega = 30E_{so}$ (single-minimum regime). The results are obtained using the one-dimensional effective low-energy Hamiltonian H_{1d} (a_s is treated as an input parameter).

interactions were compared with results for zero-range interactions, which utilized an effective coupling constant that results from integrating out the excited transverse wave guide modes, from the literature as input. It was shown that the resonance positions can be tuned by the spin-orbit coupling parameters. A parameter window was identified in which the scattering observables are essentially independent of the underlying two-body potential.

The formulation and results presented provide the starting point for future studies. It will be interesting to explore the case where the interactions in the triplet channels contribute or even dominate. It will also be interesting to apply the formalism to bosons. One question concerns the construction of an effective low-energy single-band Hamiltonian based on the effective one-dimensional coupling constants discussed in this work. Last, it will be interesting to extend the study to the three-body sector and to two-body systems with different effective spin.

VIII. ACKNOWLEDGEMENT

We would like to thank Wei Zhang for discussions. Support by the National Science Foundation through grant numbers PHY-1509892 and PHY-1745142 is gratefully acknowledged. This work used the Extreme Science and Engineering Discovery Environment (XSEDE), which is supported by NSF Grant No. OCI-1053575, and the OU Supercomputing Center for Education and Research (OSCER) at the University of Oklahoma (OU).

Appendix A: Generalized log-derivative algorithm

1. Rewriting the coupled equations

The Schrödinger equation given in Eq. (24) can be rewritten in the generic form

$$\left[\underline{I}\frac{d^2}{dz^2} - \imath\underline{\alpha}\frac{d}{dz} + \underline{\beta}(z)\right]\underline{\phi}^{(m_l)}(z) = 0, \tag{A1}$$

where $\underline{I}$ denotes the $4n_{\rm max} \times 4n_{\rm max}$ identity matrix,

$$\underline{\alpha} = \begin{pmatrix} \underline{a} & \underline{0} & \cdots & \underline{0} \\ \underline{0} & \underline{a} & & \\ \vdots & & \ddots & \\ \underline{0} & & & \underline{a} \end{pmatrix}, \tag{A2}$$

and

$$\underline{\beta}(z) = \begin{pmatrix} \underline{b}_{0,0}(z) & \underline{b}_{0,1}(z) & \cdots & \underline{b}_{0,n_{\rm max}-1}(z) \\ \underline{b}_{1,0}(z) & \underline{b}_{1,1}(z) & & \\ \vdots & & \ddots & \\ \underline{b}_{n_{\rm max}-1,0}(z) & & & \underline{b}_{n_{\rm max}-1,n_{\rm max}-1}(z) \end{pmatrix}. \tag{A3}$$

The 4×4 matrices $\underline{a}$ and $\underline{b}_{n'_\rho,n_\rho}(z)$ are given by

$$\underline{a} = k_{\rm so}\begin{pmatrix} 0 & 0 & 0 & -2 \\ 0 & 0 & 0 & 0 \\ 0 & 0 & 0 & 0 \\ -2 & 0 & 0 & 0 \end{pmatrix} \tag{A4}$$

and

$$\begin{aligned}\underline{b}_{n'_\rho,n_\rho}(z) =& \frac{m}{\hbar^2}\begin{pmatrix} E-\epsilon_{n_\rho,m_l} & 0 & 0 & 0 \\ 0 & E-\epsilon_{n_\rho,m_l}-E_{\tilde\delta} & 0 & -E_\Omega/\sqrt{2} \\ 0 & 0 & E-\epsilon_{n_\rho,m_l}+E_{\tilde\delta} & -E_\Omega/\sqrt{2} \\ 0 & -E_\Omega/\sqrt{2} & -E_\Omega/\sqrt{2} & E-\epsilon_{n_\rho,m_l} \end{pmatrix}\delta_{n'_\rho,n_\rho} - \\ & \frac{m}{\hbar^2}\begin{pmatrix} \mathcal{V}_{\rm int}^{n'_\rho,n_\rho,S_0}(z) & 0 & 0 & 0 \\ 0 & \mathcal{V}_{\rm int}^{n'_\rho,n_\rho,T_{+1}}(z) & 0 & 0 \\ 0 & 0 & \mathcal{V}_{\rm int}^{n'_\rho,n_\rho,T_{-1}}(z) & 0 \\ 0 & 0 & 0 & \mathcal{V}_{\rm int}^{n'_\rho,n_\rho,T_0}(z) \end{pmatrix}. \end{aligned} \tag{A5}$$

Dividing $\underline{\phi}^{(m_l)}(z)$ into its real and imaginary parts,

$$\underline{\phi}^{(m_l)}(z) = \underline{\phi}_{\rm re}^{(m_l)}(z) + \imath\underline{\phi}_{\rm im}^{(m_l)}(z), \tag{A6}$$

Eq. (A1) can be rewritten as a purely real matrix equation:

$$\left[\underline{I}\frac{d^2}{dz^2} + \underline{A}(z)\frac{d}{dz} + \underline{B}(z)\right]\underline{\varphi}^{(m_l)}(z) = 0. \tag{A7}$$

Here, $\underline{I}$ is of size $8n_{\rm max} \times 8n_{\rm max}$,

$$\underline{A}(z) = \begin{pmatrix} \underline{0} & \underline{\alpha} \\ -\underline{\alpha} & \underline{0} \end{pmatrix}, \tag{A8}$$

$$\underline{B}(z) = \begin{pmatrix} \underline{\beta} & \underline{0} \\ \underline{0} & \underline{\beta} \end{pmatrix}, \tag{A9}$$

and

$$\underline{\varphi}^{(m_l)}(z) = \begin{pmatrix} \underline{\phi}_{\rm re}^{(m_l)}(z) & \underline{\phi}_{\rm re}^{(m_l)}(z) \\ \underline{\phi}_{\rm im}^{(m_l)}(z) & \underline{\phi}_{\rm im}^{(m_l)}(z) \end{pmatrix}. \tag{A10}$$

In writing Eq. (A7) [see also Eq. (A10)], we "doubled" the solution, i.e., the real part $\underline{\phi}_{\rm re}^{(m_l)}(z)$ and the imaginary part $\underline{\phi}_{\rm im}^{(m_l)}(z)$ both appear twice. In our case, $\underline{A}$ is independent of z. We note, however, that the manipulations and algorithm outlined below are also valid if $\underline{A}$ depends on z, provided $\underline{A}^T$ is equal to $-\underline{A}$ [24]. To em-

phasize this, we formally indicate the z-dependence of $\underline{A}$ in what follows.

Our goal is to propagate $\underline{\varphi}^{(m_l)}(z)$ from $z_{\min}$ to $z_{\max}$, subject to appropriately chosen boundary conditions at $z_{\min}$. Since we are using Gaussian interaction potentials, the propagation starts at $z_{\min} = 0$. We write

$$\underline{\phi}_{\rm re}^{(m_l)}(0) = \begin{pmatrix} \underline{\gamma}_1 & \underline{0} & \cdots & \underline{0} \\ \underline{0} & \underline{\gamma}_1 & & \\ \vdots & & \ddots & \\ \underline{0} & & & \underline{\gamma}_1 \end{pmatrix}, \tag{A11}$$

$$\left(\frac{d}{dz}\underline{\phi}_{\rm re}^{(m_l)}(z)\right)\Big|_{z=0} = \begin{pmatrix} \underline{\gamma}_2 & \underline{0} & \cdots & \underline{0} \\ \underline{0} & \underline{\gamma}_2 & & \\ \vdots & & \ddots & \\ \underline{0} & & & \underline{\gamma}_2 \end{pmatrix}, \tag{A12}$$

$$\underline{\phi}_{\rm im}^{(m_l)}(0) = \underline{0}, \tag{A13}$$

and

$$\left(\frac{d}{dz}\underline{\phi}_{\rm im}^{(m_l)}(z)\right)\Big|_{z=0} = \underline{0}. \tag{A14}$$

The matrices $\underline{\gamma}_1$ and $\underline{\gamma}_2$ are chosen so that the total wave function has the desired exchange symmetry. For two identical fermions and even m_l quantum number, e.g., the anti-symmetry of the total wave function is fulfilled if we set

$$\underline{\gamma}_1 = \begin{pmatrix} 1 & 0 & 0 & 0 \\ 0 & 0 & 0 & 0 \\ 0 & 0 & 0 & 0 \\ 0 & 0 & 0 & 0 \end{pmatrix} \tag{A15}$$

and

$$\underline{\gamma}_2 = \begin{pmatrix} 0 & 0 & 0 & 0 \\ 0 & 1 & 0 & 0 \\ 0 & 0 & 1 & 0 \\ 0 & 0 & 0 & 1 \end{pmatrix}. \tag{A16}$$

For a two-body potential with repulsive core, $\underline{\phi}_{\rm re}^{(m_l)}$ and $d\underline{\phi}_{\rm re}^{(m_l)}/dz$ would be set to $\underline{0}$ and $\underline{I}$, respectively, at $z = z_{\min}$.

2. Formalism behind the algorithm

It is useful to define the propagators $\underline{L}^{(j)}(z', z'')$ with $j = 1 - 4$,

$$\begin{pmatrix} \underline{\varphi}'(z') \\ \underline{\varphi}'(z'') \end{pmatrix} = \begin{pmatrix} \underline{L}^{(1)}(z', z'') & \underline{L}^{(2)}(z', z'') \\ \underline{L}^{(3)}(z', z'') & \underline{L}^{(4)}(z', z'') \end{pmatrix} \begin{pmatrix} \underline{\varphi}(z') \\ \underline{\varphi}(z'') \end{pmatrix}, \tag{A17}$$

where we introduced the abbreviations $\underline{\varphi}(z') = \underline{\varphi}^{(m_l)}(z')$ and

$$\underline{\varphi}'(z') = \frac{d\underline{\varphi}^{(m_l)}(z)}{dz}\Big|_{z=z'}. \tag{A18}$$

We rearrange Eq. (A17) such that the wave function and its derivative at z'' can be, provided the propagators $\underline{L}^{(j)}(z', z'')$ are known, determined from the wave function and its derivative at z':

$$\begin{pmatrix} \underline{\varphi}(z'') \\ \underline{\varphi}'(z'') \end{pmatrix} = \begin{pmatrix} -[\underline{L}^{(2)}(z', z'')]^{-1}\underline{L}^{(1)}(z', z'') & [\underline{L}^{(2)}(z', z'')]^{-1} \\ -\underline{L}^{(4)}(z', z'')[\underline{L}^{(2)}(z', z'')]^{-1}\underline{L}^{(1)}(z', z'') + \underline{L}^{(3)}(z', z'') & \underline{L}^{(4)}(z', z'')[\underline{L}^{(2)}(z', z'')]^{-1} \end{pmatrix} \begin{pmatrix} \underline{\varphi}(z') \\ \underline{\varphi}'(z') \end{pmatrix}. \tag{A19}$$

The task is thus to find expressions for $\underline{L}^{(j)}(z', z'')$.

In the following we discuss the transformation used to express the $\underline{L}^{(j)}(z', z'')$. Following Ref. [24], we employ the transformation

$$\underline{\varphi}^{(m_l)}(z) = \underline{\mathcal{T}}(z, \bar{z})\underline{\varphi}_{\bar{z}}^{(m_l)}(z) \tag{A20}$$

to remove the first derivative with respect to z from Eq. (A7). Equation (A20) can be interpreted as switching from an adiabatic basis to a diabatic basis at each z.

Demanding that the identities

$$\left(\underline{I}\frac{d}{dz} + \frac{1}{2}\underline{A}(z)\right)\underline{\mathcal{T}}(z, \bar{z}) = \underline{0} \tag{A21}$$

and

$$\underline{\mathcal{T}}(\bar{z}, \bar{z}) = \underline{I} \tag{A22}$$

hold, Eq. (A7) becomes

$$\left[\frac{d^2\underline{\mathcal{T}}(z,\bar{z})}{dz^2}+\underline{\mathcal{T}}(z,\bar{z})\frac{d^2}{dz^2}+\underline{A}(z)\frac{d\underline{\mathcal{T}}(z,\bar{z})}{dz}+\underline{B}(z)\underline{\mathcal{T}}(z,\bar{z})\right]\underline{\varphi}_{\bar{z}}^{(m_l)}(z)=0. \tag{A23}$$

Multiplying Eq. (A23) from the left with $\underline{\mathcal{T}}^T(z,\bar{z})$, using Eq. (A21), and using that $\underline{A}(z)=-[\underline{A}(z)]^T$, we obtain

$$\left[\underline{I}\frac{d^2}{dz^2}+\underline{B}_{\bar{z}}(z)\right]\underline{\varphi}_{\bar{z}}^{(m_l)}(z)=0, \tag{A24}$$

where

$$\underline{B}_{\bar{z}}(z)=\underline{\mathcal{T}}^T(z,\bar{z})\underline{V}_{\rm eff}(z)\underline{\mathcal{T}}(z,\bar{z}) \tag{A25}$$

and

$$\underline{V}_{\rm eff}(z)=\underline{B}(z)-\frac{1}{4}\underline{A}(z)\underline{A}(z)-\frac{1}{2}\frac{d\underline{A}(z)}{dz}. \tag{A26}$$

In our case, $d\underline{A}(z)/dz$ is equal to zero and Eqs. (A21) and (A22) can be solved analytically:

$$\underline{\mathcal{T}}(z,\bar{z})=\frac{-\sin\left(k_{\rm so}(z-\bar{z})\right)}{2k_{\rm so}}\underline{A}+\begin{pmatrix}\underline{t}_D & \underline{0} & \cdots & \underline{0}\\ \underline{0} & \underline{t}_D & & \\ \vdots & & \ddots & \\ \underline{0} & & & \underline{t}_D\end{pmatrix}, \tag{A27}$$

where

$$\underline{t}_D=\begin{pmatrix}\cos\left(k_{\rm so}(z-\bar{z})\right) & 0 & 0 & 0\\ 0 & 1 & 0 & 0\\ 0 & 0 & 1 & 0\\ 0 & 0 & 0 & \cos\left(k_{\rm so}(z-\bar{z})\right)\end{pmatrix}. \tag{A28}$$

The algorithm discussed in the next section is based on the fact that the transformation from $\underline{\varphi}^{(m_l)}(z)$ to $\underline{\varphi}_{\bar{z}}^{(m_l)}(z)$ can be performed at each z.

3. Step by step algorithm

To perform the propagation of $\underline{\varphi}^{(m_l)}(z)$ and its derivative, we divide the interval $[z_{\rm min},z_{\rm max}]$ into N sectors of length $2h$. The grid points are labeled z_l, where l takes the values $0,2,\cdots,2N$. Note, however, that the algorithm also uses the "midpoints" $z_1,z_3,\cdots$. The algorithm is formulated in terms of a number of auxiliary quantities:

$$\underline{B}_{z_{l+2}}(z_{l+1})=\underline{\mathcal{T}}^T(z_{l+1},z_{l+2})\underline{V}_{\rm eff}(z_{l+1})\underline{\mathcal{T}}(z_{l+1},z_{l+2}), \tag{A29}$$

$$\underline{s}_{l,l+2}=\left[\frac{1}{4}\underline{I}-\frac{h^2}{8}\underline{B}_{z_{l+2}}(z_{l+1})\right]^{-1}, \tag{A30}$$

$$\underline{\mathcal{L}}_{l,l+2}^{(1)}=-7\underline{I}+2h^2\underline{V}_{\rm eff}(z_l)+\underline{\mathcal{T}}(z_l,z_{l+2})\underline{s}_{l,l+2}\underline{\mathcal{T}}^T(z_l,z_{l+2}), \tag{A31}$$

$$\underline{\mathcal{L}}_{l,l+2}^{(2)}=\underline{\mathcal{T}}(z_l,z_{l+2})\left(-\underline{I}+\underline{s}_{l,l+2}\right)^T, \tag{A32}$$

$$\underline{\mathcal{L}}_{l,l+2}^{(3)}=-\left(\underline{\mathcal{L}}_{l,l+2}^{(2)}\right)^T, \tag{A33}$$

$$\underline{\mathcal{L}}_{l,l+2}^{(4)}=14\underline{I}-4h^2\underline{V}_{\rm eff}(z_{l+2})-\underline{s}_{l,l+2}, \tag{A34}$$

$$\underline{\mathcal{Y}}_{0,l+2}=\left[\underline{\mathcal{L}}_{0,l}^{(4)}-\underline{\mathcal{T}}(z_l,z_{l+2})\underline{s}_{l,l+2}\underline{\mathcal{T}}^T(z_l,z_{l+2})\right]^{-1}, \tag{A35}$$

$$\underline{\mathcal{L}}_{0,l+2}^{(1)}=\underline{\mathcal{L}}_{0,l}^{(1)}+\underline{\mathcal{L}}_{0,l}^{(2)}\underline{\mathcal{Y}}_{0,l+2}\left(\underline{\mathcal{L}}_{0,l}^{(2)}\right)^T, \tag{A36}$$

$$\underline{\mathcal{L}}_{0,l+2}^{(2)}=\underline{\mathcal{L}}_{0,l}^{(2)}\underline{\mathcal{Y}}_{0,l+2}\underline{\mathcal{L}}_{l,l+2}^{(2)}, \tag{A37}$$

$$\underline{\mathcal{L}}_{0,l+2}^{(3)}=-\left(\underline{\mathcal{L}}_{l,l+2}^{(2)}\right)^T\underline{\mathcal{Y}}_{0,l+2}\left(\underline{\mathcal{L}}_{0,l}^{(2)}\right)^T, \tag{A38}$$

$$\underline{\mathcal{L}}_{0,l+2}^{(4)}=\underline{\mathcal{L}}_{l,l+2}^{(4)}-\left(\underline{\mathcal{L}}_{l,l+2}^{(2)}\right)^T\underline{\mathcal{Y}}_{0,l+2}\underline{\mathcal{L}}_{l,l+2}^{(2)}, \tag{A39}$$

$$\underline{L}^{(1)}(z_0,z_{l+2})=-\frac{1}{2}\underline{A}+\frac{1}{6h}\underline{\mathcal{L}}_{0,l+2}^{(1)}, \tag{A40}$$

$$\underline{L}^{(2)}(z_0,z_{l+2})=\frac{1}{6h}\underline{\mathcal{L}}_{0,l+2}^{(2)}, \tag{A41}$$

$$\underline{L}^{(3)}(z_0,z_{l+2})=\frac{1}{6h}\underline{\mathcal{L}}_{0,l+2}^{(3)}, \tag{A42}$$

and

$$\underline{L}^{(4)}(z_0,z_{l+2})=-\frac{1}{2}\underline{A}+\frac{1}{6h}\underline{\mathcal{L}}_{0,l+2}^{(4)}-7\underline{I}+2h^2\underline{V}_{\rm eff}(z_{l+2}). \tag{A43}$$

Note that the quantity $Y_{0,l+2}$ defined in Ref. [24] contains a typo in the non-labeled equation after Eq. (71): the 11-element should be -1 and not 1 and the 22-element should be 1 and not -1. If the typo was not corrected, the plus sign on the right hand side of Eq. (A36) would be a minus sign, and the minus sign on the right hand side of Eq. (A39) would be a plus sign.

With the above definitions, the algorithm reads:

- Initialization:

  1. Initialize $\underline{\varphi}(z_0)$ and $\underline{\varphi}'(z_0)$ [see Eqs. (A11)-(A16)].
  2. Initialize $\underline{\mathcal{L}}_{0,2}^{(j)}$ $(j = 1-4)$ using Eqs. (A31)-(A34) with $l = 0$.
  3. If desired, calculate $\underline{L}^{(j)}(z_0, z_2)$ using Eqs. (A40)-(A43) with $l = 0$ and then calculate $\underline{\varphi}(z_2)$ and $\underline{\varphi}'(z_2)$ using Eq. (A19) with $z' = z_0$ and $z'' = z_2$.

- For $l = 2, 4, \cdots, 2N-2$:

  1. Calculate $\underline{\mathcal{L}}_{l,l+2}^{(j)}$ using Eqs. (A31)-(A34).
  2. Calculate $\underline{\mathcal{Y}}_{0,l+2}$ using Eq. (A35).
  3. Calculate $\underline{\mathcal{L}}_{0,l+2}^{(j)}$ using Eqs. (A36)-(A39).
  4. If desired, calculate $\underline{L}^{(j)}(z_0, z_{l+2})$ using Eqs. (A40)-(A43) and then calculate $\underline{\varphi}(z_{l+2})$ and $\underline{\varphi}'(z_{l+2})$ using Eq. (A19) with $z' = z_0$ and $z'' = z_{l+2}$.

Appendix B: Explicit expressions for $\vec{a}^{(j)}$

The explicit expressions for $\vec{a}^{(j)}(k_{n_\rho}^{(j)})$, introduced in Eqs. (26) and (27), for $\tilde{\delta} = 0$ read

$$\vec{a}^{(1)}(k_{n_\rho}^{(1)}) = \left[E_\Omega^2 + 4\left|b(k_{n_\rho}^{(1)})\right|^2\right]^{-1/2} \begin{pmatrix} -E_\Omega \\ \sqrt{2}b(k_{n_\rho}^{(1)}) \\ \sqrt{2}b(k_{n_\rho}^{(1)}) \\ 0 \end{pmatrix}, \tag{B1}$$

$$\vec{a}^{(2)}(k_{n_\rho}^{(2)}) = \frac{1}{\sqrt{2}} \begin{pmatrix} 0 \\ -1 \\ 1 \\ 0 \end{pmatrix}, \tag{B2}$$

and

$$\vec{a}^{(3/4)}(k_{n_\rho}^{(3/4)}) = \left[N(k_{n_\rho}^{(3/4)})\right]^{-1/2} \begin{pmatrix} \pm 2b(k_{n_\rho}^{(3/4)}) \\ \pm E_\Omega/\sqrt{2} \\ \pm E_\Omega/\sqrt{2} \\ \sqrt{E_\Omega^2 + 4\left(b(k_{n_\rho}^{(3/4)})\right)^2} \end{pmatrix}, \tag{B3}$$

where

$$b(k_{n_\rho}^{(j)}) = \frac{\hbar^2 k_{\rm so} k_{n_\rho}^{(j)}}{m} \tag{B4}$$

and

$$N(k_{n_\rho}^{(3/4)}) = E_\Omega^2 + 4\left(b(k_{n_\rho}^{(3/4)})\right)^2 + \left|E_\Omega^2 + 4\left(b(k_{n_\rho}^{(3/4)})\right)^2\right|. \tag{B5}$$

In Eq. (B3), the "+" and "−" of the "±" are associated with the superscripts 3 and 4, respectively.

Appendix C: Details related to the "rotation approach"

The operator $\hat{R}$ in the singlet-triplet basis reads

$$\underline{R} = \begin{pmatrix} \underline{R}_0 & \underline{0} & \cdots & \underline{0} \\ \underline{0} & \underline{R}_0 & & \\ \vdots & & \ddots & \\ \underline{0} & & & \underline{R}_0 \end{pmatrix}, \tag{C1}$$

where

$$\underline{R}_0 = \begin{pmatrix} \cos(k_{\rm so}z) & 0 & 0 & -\imath\sin(k_{\rm so}z) \\ 0 & 1 & 0 & 0 \\ 0 & 0 & 1 & 0 \\ -\imath\sin(k_{\rm so}z) & 0 & 0 & \cos(k_{\rm so}z) \end{pmatrix}. \tag{C2}$$

Operating with $\underline{R}_0^\dagger$ on the vector that contains the singlet-triplet basis states, we obtain the rotated basis states $|R_j\rangle$:

$$|R_1\rangle = \cos(k_{\rm so}z)|S_0\rangle - \imath\sin(k_{\rm so}z)|T_0\rangle, \tag{C3}$$

$$|R_2\rangle = |T_{+1}\rangle, \tag{C4}$$

$$|R_3\rangle = |T_{-1}\rangle, \tag{C5}$$

and

$$|R_4\rangle = -\imath\sin(k_{\rm so}z)|S_0\rangle + \cos(k_{\rm so}z)|T_0\rangle. \tag{C6}$$

In the $|R_j\rangle$ basis, the operator $\hat{\Sigma}_z^2$ is diagonal with diagonal elements 1, 0, 0 and 0. This result is used in interpreting the approximate identity given in Eq. (86).

Using the basis $\{|R_1\rangle, \cdots, |R_4\rangle\}$, the matrix representation of U for $\tilde{\delta} = 0$ reads

$$\underline{U} = \begin{pmatrix} \underline{U}_0 & \underline{0} & \cdots & \underline{0} \\ \underline{0} & \underline{U}_0 & & \\ \vdots & & \ddots & \\ \underline{0} & & & \underline{U}_0 \end{pmatrix}, \tag{C7}$$

where

$$\underline{U}_0 = \frac{1}{\sqrt{2}} \begin{pmatrix} 0 & \sqrt{2} & 0 & 0 \\ -1 & 0 & -\sqrt{2}E_\Omega c_+ & \sqrt{2}E_\Omega c_- \\ 1 & 0 & -\sqrt{2}E_\Omega c_+ & \sqrt{2}E_\Omega c_- \\ 0 & 0 & (E_{\rm so} + \sqrt{c})c_+ & (-E_{\rm so} + \sqrt{c})c_- \end{pmatrix} \tag{C8}$$

with

$$c = (E_{\rm so})^2 + (2E_\Omega)^2 \tag{C9}$$

and

$$c_\pm = \left(c \pm E_{\rm so}\sqrt{c}\right)^{-1/2}. \tag{C10}$$

The basis states $|D_j\rangle$, obtained by acting with $\underline{U}_0^\dagger$ on the basis states $|R_j\rangle$, read

$$|D_1\rangle = \frac{-1}{\sqrt{2}}\left(|R_2\rangle - |R_3\rangle\right), \tag{C11}$$

$$|D_2\rangle = |R_1\rangle, \tag{C12}$$

$$|D_3\rangle = c_+\left[-E_\Omega\left(|R_2\rangle + |R_3\rangle\right) + \frac{E_{\rm so}+\sqrt{c}}{\sqrt{2}}|R_4\rangle\right], \tag{C13}$$

and

$$|D_4\rangle = c_-\left[E_\Omega\left(|R_2\rangle + |R_3\rangle\right) + \frac{-E_{\rm so}+\sqrt{c}}{\sqrt{2}}|R_4\rangle\right]. \tag{C14}$$

[1] M. Olshanii, Phys. Rev. Lett. **81**, 938 (1998), URL https://link.aps.org/doi/10.1103/PhysRevLett.81.938.

[2] D. S. Petrov, G. V. Shlyapnikov, and J. T. M. Walraven, Phys. Rev. Lett. **85**, 3745 (2000), URL https://link.aps.org/doi/10.1103/PhysRevLett.85.3745.

[3] L. Pricoupenko, H. Perrin, and M. Olshanii Eds., J. Phys. IV France **116** (2004), URL https://jp4.journaldephysique.org/articles/jp4/abs/2004/04/contents/contents.html.

[4] T. Bergeman, M. G. Moore, and M. Olshanii, Phys. Rev. Lett. **91**, 163201 (2003), URL https://link.aps.org/doi/10.1103/PhysRevLett.91.163201.

[5] B. E. Granger and D. Blume, Phys. Rev. Lett. **92**, 133202 (2004), URL https://link.aps.org/doi/10.1103/PhysRevLett.92.133202.

[6] P. Giannakeas, F. K. Diakonos, and P. Schmelcher, Phys. Rev. A **86**, 042703 (2012), URL https://link.aps.org/doi/10.1103/PhysRevA.86.042703.

[7] B. Heß, P. Giannakeas, and P. Schmelcher, Phys. Rev. A **92**, 022706 (2015), URL https://link.aps.org/doi/10.1103/PhysRevA.92.022706.

[8] Y. A. Bychkov and E. I. Rashba, J. Phys. C: Solid State Phys. **17**, 6039 (1984), URL http://stacks.iop.org/0022-3719/17/i=33/a=015.

[9] G. Dresselhaus, Phys. Rev. **100**, 580 (1955), URL https://link.aps.org/doi/10.1103/PhysRev.100.580.

[10] N. Goldman, G. Juzeliūnas, P. Öhberg, and I. B. Spielman, Rep. Prog. Phys. **77**, 126401 (2014), URL http://stacks.iop.org/0034-4885/77/i=12/a=126401.

[11] H. Zhai, Rep. Prog. Phys. **78**, 026001 (2015), URL http://stacks.iop.org/0034-4885/78/i=2/a=026001.

[12] J. Dalibard, F. Gerbier, G. Juzeliūnas, and P. Öhberg, Rev. Mod. Phys. **83**, 1523 (2011), URL https://link.aps.org/doi/10.1103/RevModPhys.83.1523.

[13] Y.-J. Lin, K. Jiménez-García, and I. B. Spielman, Nature (London) **471**, 83 (2011), URL http://dx.doi.org/10.1038/nature09887.

[14] C. V. Parker, L.-C. Ha, and C. Chin, Nat. Phys. **9**, 769 (2013), URL http://dx.doi.org/10.1038/nphys2789.

[15] L. Huang, Z. Meng, P. Wang, P. Peng, S.-L. Zhang, L. Chen, D. Li, Q. Zhou, and J. Zhang, Nat. Phys. **12**, 540 (2016), URL http://dx.doi.org/10.1038/nphys3672.

[16] Z. Wu, L. Zhang, W. Sun, X.-T. Xu, B.-Z. Wang, S.-C. Ji, Y. Deng, S. Chen, X.-J. Liu, and J.-W. Pan, Science **354**, 83 (2016), ISSN 0036-8075, URL http://science.sciencemag.org/content/354/6308/83.

[17] S. Kolkowitz, S. L. Bromley, T. Bothwell, M. L. Wall, G. E. Marti, A. P. Koller, X. Zhang, A. M. Rey, and J. Ye, Nat. Phys. **542**, 66 (2016), URL http://dx.doi.org/10.1038/nature20811.

[18] L. F. Livi, G. Cappellini, M. Diem, L. Franchi, C. Clivati, M. Frittelli, F. Levi, D. Calonico, J. Catani, M. Inguscio, et al., Phys. Rev. Lett. **117**, 220401 (2016), URL https://link.aps.org/doi/10.1103/PhysRevLett.117.220401.

[19] Y.-C. Zhang, S.-W. Song, and W.-M. Liu, Scientific Reports **4**, 4992 (2014), URL http://dx.doi.org/10.1038/srep04992.

[20] R. Zhang and W. Zhang, Phys. Rev. A **88**, 053605 (2013), URL https://link.aps.org/doi/10.1103/PhysRevA.88.053605.

[21] Q. Guan and D. Blume, Phys. Rev. A **95**, 020702 (2017), URL https://link.aps.org/doi/10.1103/PhysRevA.95.020702.

[22] P. Zhang, L. Zhang, and Y. Deng, Phys. Rev. A **86**, 053608 (2012), URL https://link.aps.org/doi/10.1103/PhysRevA.86.053608.

[23] F. Mrugała and D. Secrest, J. Chem. Phys. **78**, 5954 (1983), URL https://doi.org/10.1063/1.444610.

[24] F. Mrugała and D. Secrest, J. Chem. Phys. **79**, 5960 (1983), URL https://doi.org/10.1063/1.445778.

[25] B. Johnson, J. Comp. Phys. **13**, 445 (1973), ISSN 0021-9991, URL http://www.sciencedirect.com/science/article/pii/0021999173900491.

[26] L. W. Cheuk, A. T. Sommer, Z. Hadzibabic, T. Yefsah, W. S. Bakr, and M. W. Zwierlein, Phys. Rev. Lett. **109**, 095302 (2012), URL https://link.aps.org/doi/10.1103/PhysRevLett.109.095302.

[27] P. Wang, Z.-Q. Yu, Z. Fu, J. Miao, L. Huang, S. Chai, H. Zhai, and J. Zhang, Phys. Rev. Lett. **109**, 095301 (2012), URL https://link.aps.org/doi/10.1103/PhysRevLett.109.095301.

[28] C. Qu, C. Hamner, M. Gong, C. Zhang, and P. Engels, Phys. Rev. A **88**, 021604 (2013), URL https://link.aps.org/doi/10.1103/PhysRevA.88.021604.

[29] A. J. Olson, S.-J. Wang, R. J. Niffenegger, C.-H. Li,

C. H. Greene, and Y. P. Chen, Phys. Rev. A **90**, 013616 (2014), URL https://link.aps.org/doi/10.1103/PhysRevA.90.013616.

[30] N. Q. Burdick, Y. Tang, and B. L. Lev, Phys. Rev. X **6**, 031022 (2016), URL https://link.aps.org/doi/10.1103/PhysRevX.6.031022.

[31] B. Song, C. He, S. Zhang, E. Hajiyev, W. Huang, X.-J. Liu, and G.-B. Jo, Phys. Rev. A **94**, 061604 (2016), URL https://link.aps.org/doi/10.1103/PhysRevA.94.061604.

[32] Q. Guan, One-, Two-, and Three-Body Systems with Spin-Orbit Coupling, Ph.D. Thesis, Washington State University (2017), URL https://search.proquest.com/openview/2c3ce440c115d16916951d2cb80a37e5/1?pq-origsite=gscholar&cbl=18750&diss=y.

[33] Q. Guan and D. Blume, Phys. Rev. X **8**, 021057 (2018), URL https://link.aps.org/doi/10.1103/PhysRevX.8.021057.

[34] S.-J. Wang and C. H. Greene, Phys. Rev. A **94**, 053635 (2016), URL https://link.aps.org/doi/10.1103/PhysRevA.94.053635.

[35] M. J. Seaton, Reports on Progress in Physics **46**, 167 (1983), URL http://stacks.iop.org/0034-4885/46/i=2/a=002.

[36] C. Greene, U. Fano, and G. Strinati, Phys. Rev. A **19**, 1485 (1979), URL https://link.aps.org/doi/10.1103/PhysRevA.19.1485.

[37] C. H. Greene, A. R. P. Rau, and U. Fano, Phys. Rev. A **26**, 2441 (1982), URL https://link.aps.org/doi/10.1103/PhysRevA.26.2441.

[38] M. Aymar, C. H. Greene, and E. Luc-Koenig, Rev. Mod. Phys. **68**, 1015 (1996), URL https://link.aps.org/doi/10.1103/RevModPhys.68.1015.

[39] B. Heß, P. Giannakeas, and P. Schmelcher, Phys. Rev. A **89**, 052716 (2014), URL https://link.aps.org/doi/10.1103/PhysRevA.89.052716.

[40] M. G. Moore, T. Bergeman, and M. Olshanii, J. Phys. IV France **116**, 69 (2004), URL https://doi.org/10.1051/jp4:2004116003.

[41] K. Kanjilal and D. Blume, Phys. Rev. A **70**, 042709 (2004), URL https://link.aps.org/doi/10.1103/PhysRevA.70.042709.

[42] L. Pricoupenko, Phys. Rev. Lett. **100**, 170404 (2008), URL https://link.aps.org/doi/10.1103/PhysRevLett.100.170404.

[43] Z. Idziaszek and T. Calarco, Phys. Rev. Lett. **96**, 013201 (2006), URL https://link.aps.org/doi/10.1103/PhysRevLett.96.013201.

[44] T.-Y. Gao, S.-G. Peng, and K. Jiang, Phys. Rev. A **91**, 043622 (2015), URL https://link.aps.org/doi/10.1103/PhysRevA.91.043622.

[45] L. Zhou and X. Cui, Phys. Rev. A **96**, 030701 (2017), URL https://link.aps.org/doi/10.1103/PhysRevA.96.030701.

[46] R. Stock, A. Silberfarb, E. L. Bolda, and I. H. Deutsch, Phys. Rev. Lett. **94**, 023202 (2005), URL https://link.aps.org/doi/10.1103/PhysRevLett.94.023202.

[47] T. T. Wu and M. L. Yu, Journal of Mathematical Physics **43**, 5949 (2002), URL https://doi.org/10.1063/1.1519940.

[48] F. A. B. Coutinho, Y. Nogami, L. Tomio, and F. M. Toyama, Journal of Physics A: Mathematical and General **37**, 10653 (2004), URL http://stacks.iop.org/0305-4470/37/i=44/a=013.

[49] T. Cheon and T. Shigehara, Physics Letters A **243**, 111 (1998), ISSN 0375-9601, URL http://www.sciencedirect.com/science/article/pii/S0375960198001881.

[50] M. D. Girardeau and M. Olshanii, eprint arXiv:cond-mat/0309396 (2003).

[51] P. Naidon, E. Tiesinga, W. F. Mitchell, and P. S. Julienne, New Journal of Physics **9**, 19 (2007), URL http://stacks.iop.org/1367-2630/9/i=1/a=019.

[52] To obtain the even-z bound state energies, we use the in-line equation that is 11 lines below Eq. (10) of Ref. [4]. To obtain the odd-z bound state energies, we use Eq. (10) of Ref. [45]. The bound state energies are then determined self-consistently using the energy-dependent scattering length and scattering volume for the finite-range Gaussian potential as input. To calculate scattering lengths and scattering volumes at negative energies, the Padé approximation [57] is used.

[53] J. Mitroy, S. Bubin, W. Horiuchi, Y. Suzuki, L. Adamowicz, W. Cencek, K. Szalewicz, J. Komasa, D. Blume, and K. Varga, Rev. Mod. Phys. **85**, 693 (2013), URL https://link.aps.org/doi/10.1103/RevModPhys.85.693.

[54] T. Cheon and T. Shigehara, Phys. Rev. Lett. **82**, 2536 (1999), URL https://link.aps.org/doi/10.1103/PhysRevLett.82.2536.

[55] M. D. Girardeau, H. Nguyen, and M. Olshanii, Optics Communications **243**, 3 (2004), URL http://www.sciencedirect.com/science/article/pii/S0030401804010582.

[56] M. Valiente and N. T. Zinner, J. Phys. B **50**, 064004 (2017), URL http://stacks.iop.org/0953-4075/50/i=6/a=064004.

[57] S. A. Rakityansky, S. A. Sofianos, and N. Elander, J. Phys. A **40**, 14857 (2007), URL http://stacks.iop.org/1751-8121/40/i=49/a=017.